

ABSTRACT

MONIGLE, PATRICK W. Seismic Tremor at the 9°50'N East Pacific Rise Eruption Site. (Under the direction of Dr. DelWayne Bohnenstiehl).

Ocean bottom seismic observations within the 9°50' N region of the East Pacific Rise indicate persistent, low-amplitude tremor activity throughout the October 2003 through February 2007 period of monitoring. These signals exhibit either mono- or polychromatic spectral characteristics, with a ~6 Hz fundamental frequency and up to two harmonics. Individual events cannot be correlated between nearby (<1 km) stations, implying the presence of multiple, small-amplitude sources positioned within the shallow crust. Tremor exhibits a semi-diurnal periodicity, with some stations recording activity during times of increasing tidal extension and others detecting tremor signals during times of increasing compression. The amplitude, duration, and rate of activity also correlate positively with fortnightly changes in the amplitude of the tides. These spatio-temporal patterns are consistent with tremor generation in response to tidally modulated fluid flow within a network of shallow cracks. Tremor energy flux is spatially and temporally heterogeneous; however, there are extended periods of greater and lesser activity that can be tracked across portions of the array. Despite their shallow crustal origin, changes in tremor amplitude and spectral character occur in the months prior to a major microearthquake swarm and inferred seafloor spreading event on 22 January 2006, with an increase in the degree of correlation between tremor activity and tidal strain observed in the weeks leading up to this event. After the spreading event, two eruption-surviving stations near the axis continue to show high rates of tremor activity; whereas, these signals are suppressed at the single station recovered from the near-axis flanks. This off-axis quiescence may result from the dike-induced closing of cracks, or perhaps from the emplacement of impermeable flows near the station.

Seismic Tremor at the 9°50'N East Pacific Rise Eruption Site

by
Patrick W Monigle

A thesis submitted to the Graduate Faculty of
North Carolina State University
in partial fulfillment of the
requirements for the degree of
Master of Science

Marine, Earth, and Atmospheric Science

Raleigh, North Carolina

26 March 2009

APPROVED BY:

Dr. DelWayne Bohnenstiehl
Committee Chair

Dr. James Hibbard

Dr. Lara Wagner

BIOGRAPHY

Patrick Monigle grew up in Beverly, Massachusetts and was fascinated with the outdoors and sciences as a child. He graduated from Cum Laude from Governor's Academy in 2003 and was awarded the Park Scholarship at North Carolina State University, where he graduated Cum Laude in 2007 with a B.S. in Geology. As a graduate student under Dr. DelWayne Bohnenstiehl at NC State, he was able to explore the world of geophysics through traveling to destinations such as Tonga and Antarctica. After graduation, Patrick will be continuing his education at Oregon State University, focusing on the seismology of the Himalaya Mountains.

TABLE OF CONTENTS

LIST OF FIGURES_____	iv
LIST OF TABLES_____	v
1.0 Introduction_____	1
2.0 Study Site_____	4
3.0 Tremor Character_____	7
4.0 Methods_____	9
4.1 OBS Data_____	9
4.2 Tremor Detection_____	10
4.3 Assessment of Tidal Correlation_____	11
5.0 Data Analysis and Observations_____	13
5.1 Tidal Correlation_____	13
5.2 Pre- and Post-Eruptive Tremor Activity_____	16
6.0 Discussion_____	19
7.0 Summary and Conclusions_____	25
References_____	26
Figure Descriptions_____	32
Appendices_____	48
Appendix 1_____	49
Appendix 2_____	52
Appendix 3_____	54

LIST OF FIGURES

Figure 1. OBS Locations_____	38
Figure 2. Spectral Signature_____	39
Figure 3. Tremor Polarization_____	40
Figure 4. Energy Flux Density_____	41
Figure 5. Tidal Phase_____	42
Figure 6. High Correlation Example_____	43
Figure 7. Tidal Influences_____	44
Figure 8. Average Daily Spectral Power_____	45
Figure 9. Duration-Amplitude Distribution_____	46
Figure 10. RMS Amplitudes Preceding Eruption_____	47

LIST OF TABLES

Table 1. Tremor Detection Data and Statistics	37
---	----

1. Introduction

Seismic tremor signals are sustained harmonic ground motions that have been described extensively in association with subaerial volcanoes. These signals, which often precede eruptions, have become an increasingly important monitoring tool in subaerial volcanic systems [Konstantinou and Schlindwein, 2002; Chouet, 2003; McNutt, 2005]. The mechanisms responsible for generating tremor in these environments are not well understood; however, a number of candidate processes have been put forth, including: (a) fluid-flow-induced oscillations [e.g., Julian, 1994], (b) the excitation and resonance of fluid-filled cracks [e.g., Chouet, 1988] or magma bodies [e.g., Chouet 1985], and (c) the growth and collapse of fluid-filled bubbles due to hydrothermal boiling [e.g., Leet, 1988]. All of these mechanisms involve the interaction of magmatic or hydrothermal fluids with their surrounding host rocks.

Tremor signals also have been reported in non-volcanic settings. In some cases these signals can be linked similarly to the presence or movement of fluids or gas within a crustal reservoir. For example, the resonance of a water-CO₂ filled crack has been put forth to explain persistent tremor at shallow (<5 km) crustal depth in the central Apennines, Italy. These CO₂-rich fluids are proposed to originate from the degassing of mantle rocks at much greater depths [Piccinini and Saccorotti, 2008]. Elsewhere, within the forearc wedge offshore of Ecuador and Costa Rica, oscillating methane bubble clouds [Pontoise and Hello, 2002] and pulsed fluid release events [Brown et al., 2005] have been suggested as mechanisms for generating harmonic signals with similar time-frequency characteristics.

Harmonic tremor has even been observed in passive tectonic settings, such as the submerged portion of the Galicia margin in the northern Atlantic. Díaz et al. [2007] report a strong 6-hr periodicity of these signals, suggesting they are driven by fluid pressure transients induced by ocean tidal loading. These quarter-diurnal peaks in tremor activity occur during the interval between high and low tide, often near the time when the strain rate induced by ocean tidal loading reaches a maximum [Díaz et al., 2007].

A separate class of non-volcanic tremor has been observed at depth within some subduction zones [e.g., Obara, 2002]. Geodetic and seismic monitoring along both the Cascadia and Japanese margins indicates that tremor signals are generated preferentially during periods when a portion of the plate interface slips aseismically [Miller et al., 2002; Rogers et al., 2003; Obara et al., 2004; Shelly et al., 2007]. During these slip episodes, Coulomb stress changes associated with the solid Earth tides and ocean tidal loading have been shown to correlate with the timing of tremor activity [Shelly et al., 2007; Rubinstein et al., 2008; Nakata et al., 2008]. This idea that relatively small (10^{3-4} Pa) tidal stress changes may influence the timing of tremor-producing aseismic fault motions is an extension of the mechanism used to explain tidal triggering of seismogenic motions (earthquakes) within the shallow crust [e.g., Tanaka et al. 2002; Cochran et al., 2004; Wilcock et al., 2001; Tolstoy et al., 2002; Stroup et al., 2007].

Most relevant to this study are observations of tremor originating from submarine volcanic and hydrothermal systems in the deep ocean. Acoustic signals with harmonic characteristics have been detected at far regional distances by moored underwater hydrophones and island-based seismic stations [e.g., Talandier and Okal, 1987; Dziak and

Fox, 2002; Haxel and Dziak, 2005]. These tremor signals appear to be sourced from shallow (<800 m) volcanic seamounts, where sound may couple into and propagate efficiently within the ocean's low-velocity waveguide. They commonly are interpreted to reflect resonance within the submarine magma chamber, and sometimes exhibit a repetitive pattern, suggesting a geyser-like process [Talandier and Okal, 1996].

Local deployments of ocean bottom sensors also have recorded harmonic waveforms near the summits of both Brothers Volcano in the Kermadec Arc [Dziak et al., 2008] and Axial Volcano on the Juan de Fuca Ridge [Tolstoy et al., 2002]. Although such signals have been described as pervasive, they typically cannot be correlated between nearby stations. This observation implies the existence of multiple shallow sources that may represent resonance within a network of fluid-filled cracks, rather than within the central magma chamber that underlies these volcanic systems [Tolstoy et al., 2002; Dziak et al., 2008].

Beginning in October 2003, an array of Ocean Bottom Seismometers (OBSs) was deployed locally along the crest of the East Pacific Rise (EPR) near 9°50' N. This project was part of a RIDGE 2000 initiative to monitor hydrothermal processes along this fast-spreading mid-ocean ridge (MOR) system. A catalog of discrete microearthquake events has been generated from the first seven months of seismic monitoring [Tolstoy et al., 2008]. These data have been used to define the pattern of hydrothermal flow within the crust [Tolstoy et al., 2008], as well as delineate the size-frequency distribution [Bohnenstiehl et al., 2008] and tidally influenced temporal pattern of microearthquakes [Stroup et al., 2007].

Here we report on harmonic tremor observed by this OBS array during its full 41-month period of monitoring between October 2003 and February 2007. This time window brackets a seismically-detected seafloor-spreading event on 22 January 2006 [Tolstoy et al., 2006]. Our focus is on documenting the pattern of tremor occurrence and changes in its rate and character that may be related to both dynamic tidal strains and the static magma-induced deformation. Such documentation provides a rare opportunity to examine the long-term evolution of tremor activity within a dynamic mid-ocean ridge system and investigate what role tremor detection might play in efforts to predict future eruptive activity in the deep ocean.

2. Study Site

This study documents tremor activity recorded at a depth of ~2500 m along the fast-spreading (110 mm/yr) EPR, between ~9°49 and 9°52' N latitude (Figure 1). The area exhibits an axial high morphology, with a 50-200 m wide and 5–20 m deep axial summit trough (AST) running along its crest [Haymon et al., 1991; Fornari et al., 1998a]. Multi-channel seismic (MCS) investigations during the mid-1980's detected an axial magma chamber (AMC) reflector at ~1.4 km below the seafloor [Kent et al., 1993], and preliminary analysis of 3-D MCS data collected during the summer of 2008 indicates that a pool of melt persists beneath the site [Carton et al., 2008]. This long-lived magmatic system supports an active hydrothermal cell and the release of high and low temperature vent fluids at numerous sites along the ridge crest (Figure 1).

The area near 9°50' N has been studied in detail since the immediate aftermath of a seafloor eruption was documented during a series of submersible dives in early 1991 [Haymon et al., 1993]. Subsequent analysis of geochemical markers suggested that observations made by Haymon et al. [1993] occurred with a month of the eruption's cessation, with ^{210}Po - ^{210}Pb dating of the young lavas indicating the area was repaved by a series of eruptions during the course of a year [Rubin et al., 1994]. Time series investigations since the 1991-1992 eruptive episode have focused on tracking the pattern of biological succession [Shank et al., 1998], as well as documenting long-term changes in hydrothermal fluid temperature [Fornari et al., 1998b; Scheirer et al., 2006] and chemistry [Von Damm et al., 1995].

A previous OBS investigation by Sohn et al. [1998, 1999] recorded 283 microearthquakes beneath the 9°50' N area during a three-month period in 1995. These results indicated a concentration of cracking within the hydrothermal reservoir, where the convective mining of heat from the upper crust results in a high rate of thermal stressing. This study also elucidated the possible impact of microearthquake activity on the hydrothermal system, documenting a vent temperature perturbation of nearly +7° C that correlated spatially and temporally with a swarm of activity within the subsurface. Sohn et al. [1998, 1999], however, did not report on the occurrence of tremor activity.

The OBS data used in this study were collected during a series of four deployments between October 2003 and February 2007. Microearthquake arrivals from the first deployment (October 2003-April 2004) have been carefully analyzed to produce a catalog of more than 9,000 earthquakes [Tolstoy et al., 2008; Bohnenstiehl et al., 2008] and indicate an

order of magnitude increase in event rate relative to those observed by Sohn et al. [1998]. Precisely relocated hypocenters, obtained using the double-difference procedure of Waldhauser and Ellsworth [2000], indicate a concentration of microearthquakes occupying a 200–300 m wide zone that lies at a depth of 0.9-1.4 km beneath the AST [Tolstoy et al., 2008]. At shallow depths, Tolstoy et al. [2008] have documented a sub-vertical, pipe-like zone of microearthquake activity that is coincident with a 100 m offset in the AST near 9°49.25'N. This is interpreted to represent an on-axis down-flow zone, where cold seawater is being entrained into the crust [Tolstoy et al., 2008].

Stroup et al. [2007] has used this microearthquake catalog to show an increased rate of seismic activity during times of tidally-induced extension, with volumetric stress changes of 0.7-4.0 kPa producing a non-random temporal behavior. As the region exhibits small (<0.2 m) ocean tides, these stress changes are modulated largely by the direct solid Earth tide. However, the spatial pattern of microearthquake phase lags relative to times of peak tidal extension may require an additional poro-elastic effect that indicates high permeabilities within the interfered down flow zone and beneath the main vent field near 9°50' N [Stroup et al., 2008].

Relative to seismic rates observed during the fall of 2003, when OBS monitoring began, there is a long-term ramp-up in microearthquake activity that culminates in a massive seismic swarm on 22 January 2006. Tolstoy et al. [2006] interpreted this swarm as marking the emplacement of a dike feeding a significant eruption within the site, an observation supported by regional hydrophone recordings [Dziak et al., in review]. Seismicity rates drop

dramatically in the day and weeks following the January 2006 seismic swarm [Tolstoy et al., 2006].

Subsequent water column and seafloor observations have confirmed the presence of recent volcanism, with approximately $22 \times 10^6 \text{ m}^3$ of lava erupted onto the seabed, or <15 % of the total magma available in the AMC [Soule et al., 2007]. Short half-life (^{210}Po - ^{210}Pb) dating suggests eruptive activity beginning in June or July 2005 and terminating by January 2006, with approximately 80% of lava extruded by September 2005 [Rubin et al., 2008]. However, this observation remains at odds with both local OBS [Tolstoy et al., 2006] and regional hydroacoustic observations [Dziak et al., in review], which indicate that the site's seismic energy release is dominated by the single swarm event on 22 January 2006.

3. Tremor Character

Seismic activity along the $9^{\circ}50'N$ ridge crest is characterized by both discrete local earthquake activity and seismic tremor. Local microearthquake activity is broadband and transient, with typically short (< 2-3 s) duration wave packets consisting of distinct P- and S-phase arrivals [Tolstoy et al., 2008]. Tremor activity, however, represent a narrowband signal with a mono- or polychromatic spectral signature (Figure 2). Individual tremor packets typically extend for 10-100's of seconds and may occur in episodes lasting several hours. Although some tremor activity appears to be excited or amplified by the release of broadband energy during microearthquake events, tremor signals are most commonly observed as emergent waveforms that lack distinct phase arrivals (Figure 2).

The occurrence rate and amplitude of tremor signals are spatially heterogeneous throughout the array (Table 1). This pattern may reflect the distribution and character of the tremor sources, as well as possible differences in the degree of coupling among these drop-deployed sensors. In general, however, tremor occurrence and duration are greatest immediately along the ridge crest (Stations 1 and 9-11) (Table 1, Figure 1).

Specific packets of tremor activity cannot be correlated between stations within the array, preventing their locations from being determined and suggesting that multiple small-amplitude sources occur near each station. Despite the incoherent character of these signals, periods of increasing and decreasing activity can be seen across the array. This pattern implies that these discrete local sources are sensitive to array-scale processes.

A given packet commonly shows a consistent polarization signature (Figure 2), and for most stations the polarization remains stable during the deployment, being dominated by signals arriving from one or two azimuthal directions. These azimuths do not align to a common location, again suggesting the presence of distinct source regions near each station. For stations in close proximity to the ridge axis, however, there is a weak clustering in the direction of the high-temperature vent field (Figure 3 and Appendix 2).

The fundamental frequency of the observed tremor signals lies between 4 and 8 Hz. At individual stations, short-term fluctuations in frequency content occur over time scales ranging from 10's of seconds to minutes. This phenomenon, known as spectral gliding, may result from changing boundary conditions, which can include the dimensions of the resonating conduit and/or fluid flow rate [e.g., McNutt, 2005]. There are no sustained

differences in frequency between stations or long-term trends throughout the monitoring period. One or two harmonics are commonly observed, with monochromatic signals evolving into polychromatic signals, or vice-versa.

4. Methods

4.1. OBS Data

Four deployments of OBS instrumentation provide nearly continuous monitoring of the 9°50' N vent field between October 2003 and February 2007 (Figure 1). All instruments were drop deployed, with their positions on the seabed determined by acoustic ranging relative to the surface ship. The instrumentation deployed during the first deployment (October 2003-April 2004) consisted of a short-period (Mark Products L22) seismic sensor and an omni-direction hydrophone. The second deployment (April 2004-May 2005) collected only vertical-channel, short-period seismic data (L22), and the third (May 2005-April 2006) and fourth (April 2006-February 2007) deployments were equipped with three-component short-period seismic sensors (Mark Products L28). As it is common to all deployments, we focus our analysis on data from the short-period, vertical-channel.

Figure 1 shows the twelve unique stations occupied during one or more of the deployments, with the time-history of deployment at each station summarized in Table 1. Deployment 3 captured the eruptive activity, with many of the instruments engulfed by the fresh lava. Consequently, usable waveform data are available for only three of the seven instruments originally deployed (stations 4, 5 and 9), with intermittent recordings on station 5

and limited horizontal component data from station 9. The four deployments overlap minimally in time and space; however, there are no individual stations with a continuous record of activity throughout the monitoring period. Stations 4 and 9 represent the most complete records, as they were occupied during the first three deployments with only minor interruption. We limit our discussion of signal polarization (3-component data) to deployment four.

4.2. Tremor Detection

To examine the temporal pattern of tremor recorded on each OBS, the root-mean-square (RMS) amplitudes of the response-corrected waveforms are calculated within the 4-8 Hz frequency band. This analysis is performed using the vertical component data, which are common to all instruments. RMS amplitudes are estimated within 10-minute time windows that are non-overlapping. This is similar to the approach used to quantify tremor activity in terrestrial volcanic systems [e.g., Endo and Murray, 1991]. However, as the observed tremor signals cannot be correlated between stations, no source locations are determined and distance-corrected displacements cannot be estimated.

While waveform amplitudes within the 4-8 Hz band appear to be dominated by tremor activity, there are additional contributions from transient broadband signals, chiefly local earthquakes [Tolstoy et al., 2008] and regional T-waves [Fox et al., 2001]. To better isolate tremor activity and detect individual ‘events’, the spectrogram cross-correlation method of Mellinger and Clarke [2000] is applied to the dataset. This is implemented using the software package *Ishmael*, originally developed for bioacoustics [Mellinger, 2001].

A hat-shaped detection kernel is defined as a function of frequency. The kernel is zero-sum, with positive amplitudes assigned within the tremor band (4-8 Hz) and equal regions of negative amplitude assigned to adjacent frequencies (Appendix 1). Cross-correlating the kernel with the signal spectrogram generates a time series of recognition scores, representing the closeness of match between the tremor and the kernel. Due to the zero-sum nature of the kernel, a correlation of zero is returned for uniform background noise, as the positively and negatively correlated portions of the spectrogram exactly cancel. Similarly, non-uniform broadband signals return lower scores than tremor events. Setting the duration of the kernel at 25 s, ~180,000 tremor events were detected on 24 instruments deployed at 12 unique stations (Table 1). The start and end times of each tremor are recorded, along with its RMS amplitude within the 4-8 Hz frequency band.

Tremor energy flux density (E) also was calculated for each *Ishmael* detected tremor event. Following Madsen [2005], $E \approx \int_0^T V_{RMS}^2 dt$, where T is the tremor duration in seconds and V_{RMS} is its RMS velocity amplitude. The summed energy flux density observed at a subset of the stations is shown in Figure 4. It has been calculated within four-day windows, with two-days of overlap between windows.

4.3. Assessment of Tidal Correlation

Tidal strain was modeled using the GOTIC2 software [Matsumoto et al., 2001], which predicts both the solid Earth and ocean tidal loading (OTL) components. The effects of ocean loading are estimated by convolving the NAO.99b ocean tide model [Matsumoto et al., 2000] with the Green's functions defined from a unit point mass acting on the Earth's

surface [Farrell, 1972]. The calculations presented in this paper utilize the 21 major long- and short-period tidal constituents within NA0.99b. Unless otherwise noted, the term tidal strain will refer to the combined effects of the solid Earth tide and OTL. Positive strains indicate extension.

Tidal strains exhibit a semi-diurnal periodicity in the 9°50' N area, reaching maximum zero-to-peak strain amplitudes of 3×10^{-8} during spring tide. This strain corresponds to a volumetric stress change of $\sim \pm 2.5$ kPa (assuming a crust with $V_p=6.5$ km/s, $V_s=3.5$ km/s, $\rho=2800$ kg/m³). Because ocean tidal (sea surface) heights near 9°50' N rarely exceed 20 cm, this deformation is controlled largely by the effects of the solid Earth tide, with the time of peak crustal extension occurring approximately one hour after the peak in ocean tidal height [Stroup et al., 2007].

In order to evaluate the timing of tremor activity with respect to the tides, phase angles were assigned using the start time of each *Ishmael*-detected event. Troughs in the tidal strain time series (times of maximum volumetric compression) were assigned values of 180°, whereas peaks in the time series (time of maximum volumetric extension) were assigned values of 0° or 360° (Figure 5). Peaks and troughs were identified using a second derivative test, with phase assignments made using a linear interpolation within each half-cycle (following Tanaka et al. [2002]).

Two statistical methods are implemented to assess the tidal phase distributions. First, the Schuster test is used to evaluate the probability (p) that the tremor phase angles are randomly distributed about the unit circle [Emter, 1997]. This method has been widely used

in evaluating the tidal triggering of discrete earthquake events [e.g., Tolstoy et al., 2002; Wilcock et al., 2002; Cochran et al., 2004; Stroup et al., 2007]. The p-value is calculated as: $p = \exp(-R^2/N)$, where, R is the sum of the unit phasors representing the direction of each phase angle and N is the total number of tremor detections.

The number of tremor events within each quadrant also is tested against a binomial model that assumes a randomly occurring event has a 1:4 chance of falling within a given 90° phase window. This is accomplished by evaluating the probability of obtaining $\geq N$ successes (tremors) in a given quadrant for a population of T trials: $p = 1 - \beta_{cdf}(N, T, 0.25)$, where β_{cdf} represent the cumulative distribution function for a binomial model evaluated for a probability of 0.25. For both the binomial and Schuster tests, p-values ≤ 0.05 typically are adopted as significant [e.g., Emter, 1997; Cochran et al., 2004; Stroup et al., 2007].

5. Data Analysis and Observations

5.1. Tidal Correlation

A semi-diurnal periodicity in tremor occurrence commonly can be observed when plotting the 4-8 Hz band-passed RMS amplitudes versus time. An example is shown in Figure 6a, using data from a period of pronounced tremor activity between 15 and 19 January 2006. GOTIC2-predicted tidal strain is shown in red. During this time, strain can be seen to peak ~2 hours after the peak in RMS values (Figure 6a). Fast-Fourier Transforms (FFT) of the tidal strain and RMS time series (Figure 6b) reveal that both exhibit peak power at a frequency of 2 cycles/day. Cross-spectral analysis of these two signals indicates a correlation

coefficient of 0.91 at this frequency, with a phase lag of -57° obtained from coherence analysis (Figure 6c).

Tremor events detected using the methods of Mellinger and Clarke [2000] also are shown in Figure 6a. These detections occur during times of elevated RMS amplitude, implying that the amplitude of the band-passed RMS time series (Figure 6a) is responding to narrowband (tremor) signals, rather than broadband noise. The tremor detections shown in this example occur primarily during periods when the crust is extending (increasing strain), most often in the $270\text{-}360^\circ$ quadrant (Figure 6d). The mean resultant phase angle of these tremors is $307 \pm 5.13^\circ$ ($1\text{-}\sigma$), implying that tremor signals lag the time of peak tidal extension by -53° on average. This agrees well with the -57° lag determined through spectral coherence measurements.

The methods illustrated in Figure 6 have been applied to all available data between October 2003 and February 2007. In implementing the cross-spectral analysis (Figure 6c), tidal strain was cross-correlated with RMS amplitude within four-day windows that overlapped by two-days. The phase lag was recorded for each four-day window that exhibited a correlation value > 0.5 at a frequency of 2-cycles/day.

Application of the Schuster test indicates that tremor detections at all stations are non-randomly distributed with respect to tidal phase ($p\text{-values} < 0.001$). Both the distribution of tremor phase events and the cross-spectral results indicate a peak in tremor activity within either the $270\text{-}360^\circ$ or $90\text{-}180^\circ$ quadrant, or a bimodal distribution with significantly non-random peaks in both quadrants (Figure 7). This implies tremor signals may be generated

preferentially during times when the crust is dilating in response to the solid Earth tide (and ocean tide is high) or during times when the crust is compressing (and ocean tide is low).

The probability of randomly recording $\geq N$ tremors in a given quadrant is quantified further using the binomial model (Section 4.3) and the results are given in Table 1, with “X” representing temporally non-random behavior. Combining available data from all four deployments, Stations 3 and 4 on the near-axis eastern ridge flanks show activity dominantly during periods of increasing compressive tidal strain (90-180°). Stations 1, 6-7, and 9-11 are characterized by tremor occurrence preferentially during times of increasing extension (270-360°) and all other stations show a significantly non-random number of events within both quadrants. For this latter group of sites, the correlation is observed to switch modes through time, typically following some period with a low rate of tremor activity. Hence, there is no pronounced 6-hr periodicity, as reported by Díaz et al. [2007] along the Galicia margin.

The influence of tidal amplitude on tremor occurrence is examined by binning the number of events as a function of the tidal amplitude during the half-cycle in which it occurred. Figure 7d depicts tremor activity from stations 4 and 9 as well as a composite of all data from all stations. Regardless of whether tremor occurs dominantly during times of compression or extension, the number of detections increases approximately linearly with increasing trough-to-peak tidal strain amplitudes—ranging from ~ 0.6 events/hour to ~ 1.3 events/hour for tidal strain amplitudes between 0.25×10^{-8} and 4.5×10^{-8} . For comparison, the average tremor occurrence rate throughout the deployments is approximately 1 event/hour. If the data are expressed in terms of tremor duration or amplitude, an equivalent linear relationship is observed with respect to increasing tidal amplitudes.

5.2. Pre- and Post-Eruptive Tremor Activity

In volcanic systems, the abundance and character of tremor has been shown to vary in response to changing boundary conditions and eruptive activity. The broadband spectral content of the OBS recordings is depicted in Figure 8, using daily averages for the three eruption-surviving stations (4, 5, and 9). Prior to 22 January 2006, 4-8 Hz tremors are evident at each station. During deployment 3, there is a small decrease in tremor frequency on station 4 (off-axis) and slight increases on stations 5 and 9. However, within the context of the entire monitoring period, these fluctuations at a time-scale of several months cannot be considered unusual. Station 5 and 9 exhibit a divergence in the fundamental frequency beginning in the summer of 2005 (Figure 8). Throughout the entire 41-month period of monitoring, there is only one other instance (Station 8, April-July, 2004) where two distinct tremor bands are sustained within the 4-8 Hz frequency range for a significant period of time.

For stations in close proximity to the ridge crest (5 and 9), tremor activity within these same spectral bands continues following the 22 January eruptive event. Median tremor amplitudes decrease on both stations 5 and 9 after 22 January, from 266.71 and 896.79 to 237.85 and 768.10 nm/s, respectively. Tremor duration also decreases following the eruption on station 9, from 27.05 to 21.69 days/year, but increases on station 5 from 17.56 days/year to 21.13 days/year. Off-axis, however, there is a hiatus in activity, with no detections observed at station 4 until 25 February 2006. These events, which occur coinciding with a slight increase in local earthquake activity, contribute little power to the daily averaged

spectra (Figure 8). During the 4th deployment (April 2006-February 2007) more robust tremor activity returns and the station records events at a rate of 6.01 days/year, approaching the pre-eruptive average (9.05 days/year) for deployment 3 (Table 1). During this time, the median RMS amplitudes for the tremors are 309 nm/s, versus 440 nm/s prior to 22 January (Table 1).

Tremor energy release is spatially and temporally variable throughout the monitoring period (Figure 4), with roughly half of the deployment 2 stations recording a lull in tremor activity that extends throughout much of the deployment (Table 1, Figure 4). The flux increases near the end of deployment 2 and into deployment 3, with the highest amplitude tremor events recorded during the entire monitoring period observed on station 9 during May 2005 (Figure 4). During the roughly two-month period before the 22 January 2006 spreading event, the energy flux associated with the tremor activity is relatively high on all three stations. However, higher levels are seen at other times during the study, and the predictive value of the energy flux time series is unclear (Figure 4).

The scaling between cumulative tremor duration and amplitude has been used to characterize eruptive and non-eruptive behavior within some terrestrial volcanic systems, as tremor amplitude is sensitive to variable pressures and source geometries [e.g., Benoit et al., 2003]. This relationship is established by measuring the cumulative tremor duration at or above a given amplitude. The duration-amplitude distribution of tremor from this study is explored in Figure 9 in three-month intervals selected to delineate periods with similar scaling behaviors. Since these signals cannot be located, no distance-attenuation correction is

applied to the amplitude measurements [e.g., McNutt, 1992; Nishimura, 1995; Benoit et al., 2003]; however, they do provide a relative measure of the changes observed at each station.

This representation of the data indicates that all of the surviving deployment 3 stations exhibit their highest rate of tremor occurrence (cumulative days/year) between May and July of 2005 (Figure 9). The stations in closest proximity to the ridge axis (5 and 9) also exhibit their highest amplitudes during this time period, with the shape of the duration-amplitude distribution approaching the scale-bounded exponential model used to describe both volcanic [e.g., Benoit et al., 2003] and non-volcanic [e.g., Watanabe et al., 2007] tremor in other systems. A true exponential distribution would be characterized by a linear slope on these log-normal plots (Figure 9). This May-July period corresponds with the time of greatest energy release for stations 5 and 9 (Figure 4). For these on-axis stations, high-amplitude tremor disappears after roughly August 2005, with a similar duration-amplitude scaling observed for activity before and after the 22 January 2006 earthquake swarm (Figure 9).

Off-axis, station 4 exhibits a consistent duration-amplitude distribution between May 2005 and the eruption on 22 January 2006, with an exponential scaling matching that seen during the May through July time frame for the on-axis stations. During deployment 3, the post-eruptive rate of activity is low. When activity returns at a higher rate during deployment 4, the population shows reduced tremor amplitude and a scaling pattern similar to that seen on the near axis station during the period prior to the 22 January swarm.

On a shorter time scale, beginning on 10 January 2006, the 4-8 Hz RMS amplitudes at stations 5 and 9 (on-axis) exhibit a phase-shifted correlation with the tidal time series that

exceeds 90%. This behavior persists through 18 and 20 January, respectively (Figure 10). Throughout the entire 41-month study, this is the only period longer than four days when the correlation coefficients at any station reach this threshold. Station 4, which lies on the near-axis flanks, does not exhibit an increased correlation (Figure 10).

6. Discussion

During most of the 41-month monitoring period, 4-8 Hz tremor signals are ubiquitous throughout the OBS array; however, neither the tremor waveforms, nor their envelopes, can be correlated between closely spaced (< 1 km) stations. Because the axial magma lens lies roughly equidistant to all stations (~ 1.4 km below the seafloor) [Kent et al., 1993], this non-correlation implies that the movement of magma and resonance within the chamber are unlikely mechanisms—as sources at such depths would be expected to produce coherent arrivals across the small-aperture array. Rather, the spatially heterogeneous nature of these signals suggests that multiple, small-amplitude sources are positioned proximal to each OBS.

Locally produced tremor activity exhibiting similar characteristics have been observed during previous ocean bottom studies and these observations argue for a common source mechanism related to the movement of fluids at shallow depths. For example, observations from Axial Volcano [Tolstoy et al., 2002] and the Galicia Margin [Díaz et al., 2007] indicate monochromatic (~ 6 Hz) and polychromatic (4-10 Hz fundamental) tremor signals that appear uncorrelated between OBS stations deployed with a separation of ~ 5 km.

Similarly, at Brothers Volcano, Dziak et al. [2008] describe polychromatic (3 Hz fundamental) tremors that cannot be correlated on stations separated by as little as 2 km. The tremor signals produced at these sites also exhibit temporal changes in frequency content and/or spectral gliding, consistent with 9°50' N activities.

Waveform polarization measurements (deployments 3 and 4) show one or two dominant signal azimuths at each station, with polarization directions that cannot be aligned to a common source. Consistent polarization signatures at a given station also were observed by Díaz et al. [2007] on the Galicia Margin. At 9°50' N, however, stations clustered near the main vent field exhibit polarizations aligned roughly toward or along the axis (Figure 3). This observation, coupled with the typically greater rate of tremor occurrence for stations on-axis (Table 1), indicates that the hydrologic environment associated with the vent system may encourage tremor production. Yet, its presence in passive margin settings [e.g., Díaz et al., 2007] indicates that high-temperature flow is not required.

Tidal loading has been modeled to generate vertical and horizontal pressure gradients in hydrothermal systems as a result of spatial variations in fluid temperatures and crustal properties [Crone and Wilcock, 2005]. As a result, fluid velocities in the seafloor are predicted to vary substantially with the tides [Schultz and Elderfield, 1997]. Tide-related variability has been observed at TAG hydrothermal system along the Mid-Atlantic Ridge in which fluid release pulses were correlated with tidal strain transients [Fujioka et al., 1997]. Similarly, high-temperature fluid releases have been observed along the South Mariana Trough in response to peaks in ocean tidal loading [Sato et al., 1995].

For each of the 9°50' N stations, a semi-diurnal (~12 hr) periodicity in tremor occurrence is observed. Increased activity occurs either during times of increasing or decreasing tidal strain, typically reaching peak levels a few hours before the times of maximum extension or maximum compression. This pattern differs from that of tidally influenced microearthquake occurrence, which is characterized by increased activity surrounding the times of peak extensional stress [Stroup et al., 2007], with poro-elastic effects generating minor spatial variability in the mean phase angle ($\pm 10-20$) [Stroup et al., 2008]. Hence, the timing of the observed tremor signals appears inconsistent with a Coulomb failure model, whereby tremor is generated within the fault-zone during episodes of slip [e.g., Shelly et al., 2007; Nakata et al., 2008].

A semi-diurnal periodicity in tremor occurrence also has been observed on Axial Volcano [Tolstoy et al., 2002], although correlation with a specific tidal phase has not been analyzed in detail. On the Galicia Margin, however, Díaz et al. [2007] presented a detailed assessment of tremor occurrence with respect to a time series of sea-surface height, which can be shown to dominate the tidal strain in that region. As observed for the 9°50'N data, they report tremor production during times of increasing and decreasing strain; however, those data exhibit a 6-hr periodicity with elevated activity during each successive phase of tidal-induced compression and extension. The mechanisms controlling these different behaviors are not well understood, but may reflect changes in the local hydrology between an active ridge crest and highly sedimented passive margin.

It is conceivable that ocean bottom currents might generate tidally correlated noise; however, bottom mounted acoustic Doppler current profiler (ADCP) data collected by

Adams and Mullineaux [2008] show a pronounced quarter-diurnal periodicity that is not observed in the tremor records (Figure 6b and Appendix 1). Karman vortex shredding, a narrow band signal associated with strong ocean bottom currents [e.g., Duennebieer et al., 1981], also is unlikely because currents along the 9°50' N ridge crest rarely approach its ~10 cm/s threshold [Adams and Mullineaux, 2008]. Rather, these tremor observations are consistent with fluid-flow induced oscillations [e.g., Julian, 1994] or resonance [Chouet et al., 1998] within a network of shallow cracks. The temporal pattern of tremor activity strongly suggests that this fluid-flow is driven by dynamic tidal strains and loading, with larger amplitude tides generating stronger tremor signals of longer duration.

Earth tide induced extension, coupled with a small increase (typically < 20 cm) sea-surface tidal height, should favor the movement of fluids into the crust. Whereas, crustal compression, coupled with a period of low ocean tide, should cause crustal fluids to be expelled. Microearthquake patterns and the distribution of vent sites have been used to establish that the overall pattern of hydrothermal circulation in the area is dominated by down-welling focused near an offset located at 9°49.25' N and upwelling beneath a high-temperature field centered near 9°50' N [Tolstoy et al., 2008]. However, with respect to its generation during times of increasing extension or compression, the pattern of tremor occurrence is more heterogeneous, suggesting that it is largely decoupled from this deeper pattern of hydrothermal circulation.

Beginning in May 2005, stations 5 and 9 (on-axis) exhibit a near simultaneous divergence into two frequency bands within the 4-8 Hz frequency range (Figure 8), with a drift in fundamental frequency observed on all three of the stations available for deployment

3. Small changes in the fundamental frequency could result from continued deformation of the upper crustal layer, resulting in a change in the dimensions of the conduit, or potentially a change in the temperature of the fluids within. Long-term changes in the tremor's fundamental frequency are observed at other times during the experiment; hence, these observations need not represent a precursor to the spreading event. More unusual is the formation of a second sustained tremor band in the 4-8 Hz range at both stations 5 and 9. This occurrence is interpreted to mark the opening of new cracks (source regions) or reopening of conduits previously sealed by mineral deposition. Also, during this period, the largest observed tremor amplitudes are recorded at station 9 (Figure 4), suggesting that the tremor (despite the upper crustal origin) may be tracking an early stage of pre-eruptive deformation.

Although these changes in tremor characteristics occur just before the onset of eruptive activity cited by Rubin et al. [2008] from the analysis of short half-life isotopes (late June through early July), the absence of significant broad-band seismic activity is inconsistent with these changes marking the onset of eruptive activity (Figure 8). As noted by Tolstoy et al. [2006], seismic energy release is dominated by the 22 January swarm (Figure 8).

Within a time period of a few weeks before this swarm, on-axis tremor activity exhibits its highest correlation to tidal strain. Although the signals remain out of phase, a correlation of >90% is observed during an eight-day time span (Figure 10). Coincident with this observation, temperature loggers in the high-temperature M-vent (~9°51'N) record steadily decreasing temperatures on 9 January from background values of 360°C to values

below the 150°C monitoring threshold. These changes occur during a period of less than six hours [Von Damm et al., in review]. Also during this time window, two regional hydrophones near 110°W, 8°N and 95°W, 8°N detected a series of ~250 small-magnitude (likely $M_L < 2.0$) T-wave signals [Dziak et al., in review]. Although these events cannot be accurately located, they appear to be sourced in vicinity of the broader 9°50' N region. These observations suggest that there exists a precursory phase of deformation prior to rapid dike intrusion and eruption.

In the days following the eruption, earthquake activity returns to background levels [Tolstoy et al., 2006; Dziak et al., in review] and during the course of February, hydrothermal vent temperatures increase to values above background levels [Von Damm et al., in review]. Tremor activity continues along the ridge axis at durations and amplitudes similar to those immediately preceding the eruption; however, tremor activity off-axis is suspended for a month and does not return in earnest until April 2006 (Figures 8 and 9). The inferred diking event on 22 January 2006 [Tolstoy et al., 2006] likely resulted in an input of heat energy and the opening of cracks and conduits as the dike cooled along the ridge axis, allowing for continued tremor activity. Off-axis however, tremor cessation is likely the result of the closure of cracks and conduits resulting from the stress field associated with dike injection [e.g., Curewitz and Karson, 1998]. Alternatively, maps of lava distribution indicate that flows extended off-axis, very near station 4 [Soule et al., 2007]. If these flows remained unfractured for some period of time, they may have sealed existing conduits and altered the hydrology of the upper most crust.

7. Summary and Conclusions

Tremor recorded along the EPR ridge crest exhibits a mono- or polychromatic spectral signature with a fundamental frequency near 6 Hz and individual tremor packets extending for 10's to 100's of seconds. Tremor occurrence and amplitude are heterogeneous throughout the array, requiring the existence of multiple small amplitude sources in the vicinity of individual OBS stations. The spatial and temporal variability of tremor indicates it is likely the result of fluid flow in shallow subsurface cracks and conduits.

Each of the 9°50' N stations exhibits a semi-diurnal periodicity of tremor occurrence associated with increasing or decreasing tidal strain, with peak levels of tremor activity typically occurring a few hours before times of maximum compression or extension. This temporal pattern suggests that fluid-flow in the shallow crust is driven by tidal strain transients, as larger tidal strains generate greater tremor occurrence with larger amplitudes and longer duration.

Tremor rate and character also respond to the static magma induced deformation associated with eruptive activity. Deployments bracketing the eruption exhibit typically greater median RMS amplitudes and higher duration, resulting in increased energy flux. Tremor activity exhibits its greatest tidal correlations in the weeks preceding the eruption, which helps to define a three-week precursory period that may signal imminent eruption on the ridge crest. Post-eruption, a suspension of tremor activity off-axis suggests the stress field associated with the dike injection or local lava flows closed cracks and conduits, while on-axis tremor continues with similar characteristics.

References

- Adams, D.K., and L.S. Mullineaux (2008), Supply of gastropod larvae to hydrothermal vents reflects transport from local larval sources, *Limnol. Oceanogr.*, *53* (5), 1945-1955.
- Benoit, J. P., S. R. McNutt, and V. Barboza (2003), Duration-amplitude distribution of volcanic tremor, *J. Geophys. Res.*, *108*(B3), 2146, doi:10.1029/2001JB001520.
- Bohnenstiehl, D. R., F. Waldhauser, and M. Tolstoy (2008), Frequency-magnitude distribution of microearthquakes beneath the 9° 50' N region of the East Pacific Rise, October 2003 through April 2004, *Geochem. Geophys. Geosyst.*, *9*, Q10T03, doi:10.1029/2008GC002128.
- Brown, K. M., M. D. Tryon, H. R. DeShon, L. M. Dorman, and S. Y. Schwartz (2005), Correlated transient fluid pulsing and seismic tremor in the Costa Rica subduction zone, *Earth Planet. Sci. Lett.*, *238* (1-2), 189-203, doi:10.1016/j.epsl.2005.06.055.
- Carton, H., et al., (2008), Characteristics of the crustal magma body in the 2005-2006 eruption area at 9°50'N on the East Pacific Rise from a 3D multi-channel seismic investigation, *EOS Trans. AGU*, *89* (53), Fall Meet. Suppl., Abstract B23F-03.
- Chouet, B. (1985), Long-period volcano seismicity: its source and use in eruption forecasting, *Nature*, *380*, 309-316, doi:10.1038/380309a0.
- Chouet, B. (1988), Resonance of a Fluid-Driven Crack: Radiation Properties and Implications for the Source of Long-Period Events and Harmonic Tremor, *J. Geophys. Res.*, *93*(B5), 4375-4400.
- Chouet, B. (2003), Volcano Seismology, *Pure Appl. Geophys.*, *160*, 739-788.
- Cochran, E. S., J. E. Vidale, and S. Tanaka (2004), Earth tides can trigger shallow thrust fault earthquakes, *Science*, *306* (5699), 1164-1166, doi:10.1126/science.1103961.
- Crone, T.J., and W.S.D. Wilcock (2005), Modeling the effects of tidal loading on mid-ocean ridge hydrothermal systems, *Geochem., Geophys., Geosys.*, *6* (7), doi:10.1029/2004GC000905.
- Curewitz, D. and J.A. Karson (1998), Geological consequences of dike intrusion at mid-ocean ridge spreading centers, in *Faulting and Magmatism at Mid-Ocean Ridges*, edited by Buck, W.R., Delaney, P.T., Karson, J.A., and Lagabriele, Y., Geophysical Monograph, 106, 117-136.
- Díaz, J., J. Gallart, and O. Gaspa (2007), Atypical seismic signals at the Galicia Margin, North Atlantic Ocean, related to the resonance of subsurface fluid-filled cracks, *Tectonophysics*, *433* (1-4), 1-13, doi:10.1016/j.tecto2007.01.004.
- Duennebier, F. K., G. Blackinton, and G. Sutton (1981), Current-generated noise recorded on ocean bottom seismometers, *Marine Geophys. Res.*, *5* (1), 109-115, doi:10.1007/BF00310316.

- Dziak, R. P., and C. G. Fox (2002), Evidence of harmonic tremor from a submarine volcano detected across the Pacific Ocean basin, *J. Geophys. Res.*, *107*(B5), 2085, doi:10.1029/2001JB000177.
- Dziak, R. P., J. H. Haxel, H. Matsumoto, T. K. Lau, S. G. Merle, C. E. J. de Ronde, R. W. Embley, and D. K. Mellinger (2008), Observations of regional seismicity and local harmonic tremor at Brothers volcano, south Kermadec arc, using an ocean bottom hydrophone array, *J. Geophys. Res.*, *113*, B08S04, doi:10.1029/2007JB005533.
- Dziak R.P., D.R. Bohnenstiehl, H. Matsumoto, M.J. Fowler, J. H. Haxel, and M. Tolstoy (in review), The January 2006 seafloor-spreading event at 9° 50' N, East Pacific Rise: Ridge dike intrusion and transform fault interactions from regional hydroacoustic data, Submitted *Geochem., Geophys., Geosys.*.
- Emter, D. (1997), Tidal triggering of earthquakes and volcanic events, in *Tidal Phenomenon*, edited by H. Wilhelm, et al., Berlin, Springer-Verlag, 293-309.
- Endo, E. T., and T. Murray (1991), Real-time seismic amplitude measurement (RSAM): a volcano monitoring and prediction tool, *Bull. Volcanol.*, *53* (7), 533-545, doi: 10.1007/BF00298154
- Farrell, W. E. (1972), Earth tides, ocean tides and tidal loading, *Philosophical Trans. of the Royal Soc. of London*, *274* (1239), 253-259, doi:10.1098/rsta.1973.0050.
- Fornari, D.J., R.M. Haymon, M.R. Perfit, T.K.P Gregg, and M.H. Edwards (1998a), Axial summit trough of the East Pacific Rise 9°-10°N: geological characteristics and evolution of the axial zone on fast spreading mid-ocean ridges, *J. Geophys. Res.*, *103* (B4), 9827-9855.
- Fornari, D.J., T. Shank, K. L. Von Damm, T. K. P Gregg, M. Lilley, G. Levai, A. Bray, R. M. Haymon, M. R. Perfit, and R. Lutz (1998b), Time-series temperature measurements at high-temperature hydrothermal vents, East Pacific Rise 9°49'-51'N: evidence for monitoring a crustal cracking event, *Earth Planet. Sci. Lett.*, *160* (3-4), 419-431, doi:10.1016/S0012-821X(98)00101-0.
- Fox, C. G., H. Matsumoto, and T.-K. A. Lau (2001), Monitoring Pacific Ocean seismicity from an autonomous hydrophone array, *J. Geophys. Res.*, *106*(B3), 4183-4206.
- Fujioka, K., K. Kobayashi, K. Kato, M. Aoki, K. Mitsuzawa, M. Kinoshita, and A. Nishizawa (1997), Tide-related variability of TAG hydrothermal activity observed by deep-sea monitoring system and OBSH, *Earth Planet. Sci. Lett.*, *153* (3-4), 239-250, doi:10.1016/S0012-821X(97)00174-X.
- Haymon, R.M., D. J. Fornari, M. H. Edwards, S. Carbotte, D. Wright, and K. C. Macdonald (1991), Hydrothermal vent distribution along the East Pacific Rise crest (9°09'-54'N) and its relationship to magmatic and tectonic processes on fast-spreading mid-ocean ridges, *Earth Planet. Sci. Lett.*, *104* (2-4), 513-534, doi:10.1016/0012-821X(91)90226-8.

- Haymon, R.M., D.J. Fornari, K.L. Von Damm, M.D. Lilley, M.R. Perfit, J.M. Edmond, W.C. Shanks III, R.A. Lutz, J.M. Grebmeier, S. Carbotte, D. Wright, E. McLaughlin, M. Smith, N. Beedle, and E. Olson (1993), Volcanic eruption of the mid-ocean ridge along the East Pacific Rise crest at 9°45-52'N: Direct submersible observations of seafloor phenomena associated with an eruption event in April, 1991, *Earth and Planet. Sci. Lett.*, *119* (1-2), 85-101, doi:10.1016/0012-821X(93)90008-W.
- Haxel, J. and R. Dziak (2005), Evidence of explosive seafloor volcanic activity from the Walvis Ridge, South Atlantic Ocean, *Geophys. Res. Lett.*, *32* (13), doi:10.1024/2005GL023205.
- Julian, B. R. (1994), Volcanic tremor: Nonlinear excitation by fluid flow, *J. Geophys. Res.*, *99*(B6), 11,859–11,877.
- Kent, G.A., A.J. Harding, and J. A. Orcutt (1993), Distribution of magma beneath the East Pacific Rise between the Clipperton transform and the 9°17'N deval from forward modeling of common depth point data, *J. Geophys. Res.*, *98* (B8), 13945-13970.
- Konstantinou, K. I. and V. Schlindwein (2002), Nature, wavefield properties and source mechanism of volcanic tremor: a review, *J. Volcanol. Geotherm. Res.*, *119* (1-4), 161-187, doi:10.1016/S0377-0273(02)00311-6.
- Leet, R.C. (1988), Saturated and subcooled hydrothermal boiling in groundwater flow channels as a source of harmonic tremor, *J. Geophys. Res.*, *93* (B5), 4835-4849.
- Madsen, P.T. (2005), Marine mammals and noise: Problems with root mean square sound pressure levels for transients, *J. Acoust. Soc. Am.*, *117* (6), doi:10.1121/1.1921508.
- Matsumoto, K., T. Takanezawa, and M. Ooe (2000), Ocean tide models developed by assimilating TOPEX/POSEIDON altimeter data into hydrodynamic model: A global model and a regional model around Japan, *J. Oceanogr.*, *56*, 243-248.
- Matsumoto K., T. Sato, T. Takanezawa, and M. Ooe (2001), GOTIC2: A program for computation of oceanic tidal loading effect, *J. Geod. Soc. Japan*, *47*, 243-248.
- McNutt, S.R. (1992), Volcanic tremor, in *Encyclopedia of Earth Systems Science*, *4*, Academic Press, San Diego, California, 417-425.
- McNutt, S.R. (2005), Volcanic Seismology, *An. Rev. Earth and Planet. Sci.*, *33*, 461-491, doi:10.1146/annurev.earth.33.092203.122459.
- Mellinger, D. K. (2001), Ishmael 1.0 User's Guide, NOAA Technical Memorandum OAR PMEL-120, available from *NOAA/PMEL*, 7600 Sand Point Way NE, Seattle, WA 98115-6349.
- Mellinger, D. K, and C. W. Clark (2000), Recognizing transient low-frequency whale sounds by spectrogram correlation, *Acoust. Soc. of America*, *107* (6), 3518-3529.
- Miller, M. M., T. Melbourne, D. J. Johnson, and W. Q. Sumner (2002), Periodic slow earthquakes from the Cascadia subduction zone, *Science*, *295* (5564), 2423, doi:10.1126/science.1071193.

- Nakata, R., N. Suda, and H. Tsuruoka (2008), Non-volcanic tremor resulting from the combined effect of the Earth tides and slow slip events, *Nature Geosci.*, *1* (10), 676-678, doi:10.1038/ngeo288.
- Nishimura, T., H. Hamaguchi, and S. Ueki (1995), Source mechanisms of volcanic tremor and low-frequency earthquakes associated with the 1988-89 eruptive activity of Mt Tokachi, Hokkaido, Japan, *Geophys. J. Int.*, *121* (5), 444-458, doi: 10.1111/j.1365-246X.1995.tb05725.x.
- Obara, K. (2002), Nonvolcanic deep tremor associated with subduction in southwest Japan, *Science*, *296* (5573), 1679, doi:10.1126/science.1070378.
- Obara, K., H. Hirose, F. Yamamizu, and K. Kasahara (2004), Episodic slow slip events accompanied by non-volcanic tremors in southwest Japan subduction zone, *Geophys. Res. Lett.*, *31*, L23602, doi:10.1029/2004GL020848.
- Piccinini, D., and G. Saccorotti (2008), First observations of non-volcanic, long-period seismicity in the central Apennines, Italy, *Geophys. Res. Lett.*, *35*, L12303, doi:10.1029/2008GL034120.
- Pontoise, B., and Y. Hello (2002), Monochromatic infra-sound waves recorded offshore Ecuador: possible evidence of methane release, *Terra Nova*, *14* (6), 425-435, doi: 10.1046/j.1365-3121.2002.00437.x.
- Rogers, G and H. Dragert (2003), Episodic tremor and slip on the Cascadia subduction zone: The chatter of silent slip, *Science*, *300* (5627), 1942, doi:10.1126/science.1084783.
- Rubin, K.H., J. D. McDougall, and M. R. Perfit (1994), ^{210}Po - ^{210}Pb dating of recent volcanic eruptions on the sea floor, *Nature*, *368*, 841-844.
- Rubin, K.H., M. Tolstoy, D.J. Fornari, R.P. Dziak, S.A. Soule, F. Waldhauser, K.L. Von Damm, (2008) Integrating Radiometric, Geophysical and Thermal Signals of Volcanic Unrest and Eruption in 2005-06 at 9°50'N EPR, *Eos Trans. AGU*, *89*, Fall Meet. Suppl., Abstract # B23F-07.
- Rubinstein, J. L., M. La Rocca, J. E. Vidale, K. C. Creager, and A. G. Wech (2008), Tidal modulation of nonvolcanic tremor, *Science*, *319* (5860), 186, doi:10.1126/science.1150558.
- Sato, T., J. Kasahara, and K. Fujioka (1995), Observation of Pressure Change Associated with Hydrothermal Upwelling at a Seamount in the South Mariana Trough Using an Ocean Bottom Seismometer, *Geophys. Res. Lett.*, *22*(11), 1325–1328.
- Scheirer, D.S., T.M. Shank, and D.J. Fornari (2006), Temperature variations at diffuse and focused flow hydrothermal vent sites along the northern East Pacific Rise, *Geochem. Geophys. Geosys.*, *7* (3), doi:10.1029/2005GC001094.
- Schultz, A., and H. Elderfield (1997), Controls on the physics and chemistry of seafloor hydrothermal circulation, *Royal Society of London Phil. Trans.*, *355*, 387-425.

- Shank, T. M., D. J. Fornari, K. L. Von Damm, M. D. Lilley, R. M. Haymon, and R. A. Lutz (1998), Temporal and spatial patterns of biological community development at nascent deep-sea hydrothermal vents (9°50'N, East Pacific Rise), *Deep Sea Res. Part II: Top. Stud. in Ocean.*, *45* (1-3), 465-515, doi:10.1016/S0967-0645(97)00089-1.
- Shelly, D.R., G.C. Beroza, and S. Ide (2007), Complex evolution of transient slip derived from precise tremor locations in western Shikoku, Japan, *Geochem. Geophys. Geosyst.*, *8* (7133), doi:10.1029/2007GC001640.
- Sohn, R.A., D.J. Fornari, K.L. von Damm, J.A. Hildebrand, and S.C. Webb (1998), Seismic and hydrothermal evidence for a cracking event on the East Pacific Rise crest at 9°50'N, *Nature*, *396* (6707), 159-161.
- Sohn, R. A., J.A. Hildebrand, S.C. Webb (1999), A microearthquake survey of the high-temperature vent fields on the volcanically active East Pacific Rise (9°50'N), *J. Geophys. Res.*, *104* (205), 25,367-25378.
- Soule, S.A., D.J. Fornari, M.R. Perfit, and K.H. Rubin (2007), New insights into mid-ocean ridge volcanic processes from the 2005-2006 eruption of the East Pacific Rise, 9°46'N-9°56'N, *Geology*, *35* (12), 1079-1082, doi:10.1130/G23924A.1.
- Stroup, D. F., D. R. Bohnenstiehl, M. Tolstoy, F. Waldhauser, and R. T. Weekly (2007), Pulse of the seafloor: Tidal triggering of microearthquakes at 9°50'N East Pacific Rise, *Geophys. Res. Lett.*, *34*, L15301, doi:10.1029/2007GL030088.
- Stroup, D. F., M. Tolstoy, T.J. Crone, A. Malinverno, D. R. Bohnenstiehl, and F. Waldhauser (2008), Tidal triggering of microearthquakes constrains permeability at 9°50'N East Pacific Rise, *Eos Trans. AGU*, *89* (53), Fall Meet. Suppl., Abstract # B21A-0324.
- Talandier, J., and E.A. Okal (1987), Seismic detection of underwater volcanism: The example of French Polynesia, *Pure Appl. Geophys.*, *125* (6), 919-950, doi:10.1007/BF00879361.
- Talandier, J., and E.A. Okal (1996), Monochromatic T waves from underwater volcanoes in the Pacific Ocean: Ringing witnesses to geyser processes, *Bull. Seis. Soc. of Am.*, *86* (5), 1529-1544.
- Tanaka, S., M. Ohtake, and H. Sato (2002), Evidence for tidal triggering of earthquakes as revealed from statistical analysis of global data, *J. Geophys. Res.*, *107* (B10), doi:10.1029/2001JB001577.
- Tolstoy, M., F.L. Vernon, J.A. Orcutt, and F.K. Wyatt (2002), Breathing of the seafloor: Tidal correlations of seismicity at Axial volcano, *Geology*, *30* (6), 503-506.
- Tolstoy, M., et al. (2006), A seafloor spreading event captured by seismometers, *Science*, *314*, 1920-1922, doi:10.1126/science.1133950.
- Tolstoy, M., F. Waldhauser, D.R. Bohnenstiehl, R.T. Weekly, and W.-Y. Kim (2008), Seismic identification of along-axis hydrothermal flow in the East Pacific Rise, *Nature*, *451*, 181-184, doi:10.1038/nature06424.

- Von Damm, K.L., S.E. Oosting, R. Kozlowski, L.G. Buttermore, D.C. Colodner, H.N. Edmonds, J.M. Edmond, and J.M. Grebmeier (1995), Evolution of East Pacific Rise hydrothermal vent fluids following a volcanic eruption, *Nature*, 375, 47-50, doi:10.1038/375047.
- Von Damm, K.L., F. Prado, F. McDermott, J. Bryce, M. Lilley, T. Shank, D. Fornari (in review), Vent fluid temperature time-series data and correlative data pre- and post-eruption for high-temperature vents at the East Pacific Rise 9° 50'N, *Geochem. Geophys. Geosyst.*.
- Waldhauser, F., and W.L. Ellsworth (2000), A double-difference earthquake location algorithm: Method and application to the Northern Hayward Fault, California, *Bull. Seism. Soc. of America*, 90 (6), 1353-1368, doi:10.1785/0120000006.
- Watanabe, T., Y. Hiramatsu, and K. Obara (2007), Scaling relationship between the duration and the amplitude of non-volcanic deep low-frequency tremors, *Geophys. Res. Lett.*, 34, doi:10.1029/2007GL029391.
- Wilcock, W.S.D., S.D. Archer, and G.M. Purdy (2001), Microearthquakes on the Endeavour segment of the Juan de Fuca Ridge, *J. Geophys. Res.*, 107 (B12), 2236, doi:10.1029/2001JB000505.

Figures

Figure 1. Locations of the 12 unique OBS stations along the ridge crest plotted along with locations of known high-temperature hydrothermal vent systems (red stars). Black diamonds denote stations dominated by tremor occurrence during periods of extensional strain. Green diamonds denote stations dominated by tremor occurrence during periods of compressional strain. Blue diamonds denote stations in which tremor occurrence is temporally nonrandom in both extensional and compressional strain regimes. The periods of active monitoring at each station are in Table 1. Gray lines denote the AST [Fornari et al., 1998a].

Figure 2. Typical tremor activity recorded on OBS stations. Spectra was recorded on station 4 (deployment 3) on 4 May 2005 at 20:47:28 a) X, Y, and Z-components of seismic signal. b) Shows spectral signature of tremor with fundamental frequency near 6 Hz and harmonic near 12 Hz. Spectrogram parameters are: hamming window length of 512 samples with a 256 sample overlap, using 512 frequency points in the Fourier transform at a sampling frequency of 125 Hz. c) Spectral power ($(\text{nm/s})^2/\text{Hz}$) for 500-second window shown in spectrogram. Spectral power density is estimated using a boxcar window of the sample length and a zero-padded FFT with the next greatest power of 2 sample points. d) The instantaneous polarization on the X-Y plane in time.

Figure 3. Polarization results for all fourth deployment stations. Station orientations determined from the analysis of regional earthquake signals (Appendix 2). Stations 7 and 11

exhibit two dominant polarization azimuths. Red stars represent locations of known high-temperature hydrothermal vent systems and grey lines denote the AST [Fornari et al., 1998a].

Figure 4. Energy flux density ($\text{dB nm}^2/\text{s}$) within Ishmael-detected tremor events integrated over four-day windows with 50% overlap. Figures a-d show stations 1, 4, 5 and 9, respectively. The date of the 22 January 2006 seismic swarm is denoted with a red line. Rubin et al.'s [2008] proposed period of eruption initiation based on $^{210}\text{Po}/^{210}\text{Pb}$ data is marked with grey lines. Station 5 recorded the eruption, but was not occupied at any other time. As a result, stations 10 and 11 are included in the plot for comparison purposes, as these are the stations in closest proximity to station 5. The highest energy flux is observed on station 9 in May 2005.

Figure 5. Cartoon illustrating a 36-hour window of the tidal strain time series. The tidal phase of each individual tremor detection is determined by assigning a phase angle based on the start time of the tremor event. Phase angles are assigned based on 180° as the peak in compressional strain for a given tidal cycle, with 0° or 360° denoting the peak in extensional strain. Phase is assigned independent of strain value.

Figure 6. An example of a four-day interval with a high correlation between RMS amplitudes and tidal strain. All of the data presented were recorded by on-axis station 9 between 15 and 19 January 2006 (deployment 3). a) RMS velocity amplitude shown in blue.

Tidal strain is plotted in red and ranges $\pm 2.5 \times 10^{-8}$. Tremor detections are plotted as individual “x”. b) Fast Fourier Transform (FFT) of tidal strain (red) and RMS amplitude (blue), both exhibiting peak spectral power at ~ 2 -cycles/day. c) Cross-spectral power analysis shows RMS-amplitude and tidal strain exhibit 0.91 correlation at the frequency of 2-cycles/day. d) Rose diagram depicting the tidal phase associated with each of the 489 tremor events plotted in A. The mean phase angle is 307° with a Schuster p-value of $\ll 0.001$ (significant non-random temporal occurrence).

Figure 7. Rose diagrams depicting the phase of each Ishmael-detected tremor (blue) and RMS phase lag for all 4-day periods exhibiting a correlation > 0.5 (red). The latter is scaled 60x. a) Tremor activity at station 4, which peaks during periods of compressional strain, with a mean resultant phase angle of 139° . b) Tremor recorded at station 9, which peaks during periods of extension, with a mean resultant phase of 307° . c) A composite of tremor activity from all stations with tremor occurrence dominantly during periods of both increasing extensional and compressional strain. d) Tremor occurrence rates for stations 4 (red), 9 (black) and a mean of all stations (blue). Occurrence rates were binned based on the strain amplitude during the tidal half-cycle in which the event occurred and are normalized based on total time within each amplitude bin. Tremor amplitude and duration (not shown) exhibit a similar positive linear trend with respect to increasing tidal amplitude.

Figure 8. Average daily spectral signature for the three eruption surviving (deployment 3) stations: a) station 4 off-axis, b) station 5 on-axis, and c) station 9 on-axis. Each vertical slice represents the average spectral signal from one 24-hour monitoring period, which is established using Welch's method with 1-hour non-overlapping windows. Gray shaded areas represent gaps in data coverage. The large amplitude broadband signals observed on 22 January 2006 are unique to all four deployments and have been interpreted to represent brittle failure in response to dike intrusion [Tolstoy et al., 2006]. Notably there are no 6 Hz tremors immediately following the eruption on station 4.

Figure 9. a-c) Duration-amplitude distributions of deployment 3 tremor activity recorded on stations 4, 5 and 9, respectively. Blue represents activity between May and July 2005. Red represents activity between August 2005 and October 2005, during which time there is no data available for station 5. Black denotes the period between November 2005 and 22 January 2006, with the activity between 23 January and April 2006 shown in green. For station 4, which was reoccupied during the 4th deployment, data from April 2006-February 2007 also are shown in magenta. Durations have been normalized based on the length of each monitoring period and are in units of cumulative days of tremor per year of observation.

Figure 10. a-c) 10-minute RMS amplitudes in the 4-8 Hz band, plotted in blue, for stations 4, 5, and 9 in the two-weeks preceding the 22 January 2006 microearthquake swarm [Tolstoy et al., 2006]. Tidal strain is plotted in red and as a maximum range of $\pm 2.5 \times 10^{-8}$. These values

are typical of those values seen during other periods of spring tide. Beginning on 10 January, the phase-shifted correlation between the RMS velocity amplitudes and the tidal time series are greater than 0.90 for station 5 (through 18 January) and station 9 (through 20 January).

The 22 January 2006 swarm occurs during the neap tide.

Table 1. Tremor Detection Data and Statistics

Stations	Start Day (yyyy-ddd)	End Day (yyyy-ddd)	Total Events	Tremor Duration (days/year)	Mean Events/hour	Median Amplitude (nm/s)	Mean Energy Density Flux dB (nm ² /s)/day	Mean Phase	βcdf 90-180	βcdf 270-360
Deployment 1										
1	2003-274	2004-111	12106	23.48	2.44	211.60	87.36	317	R	X
2	2003-274	2004-111	5999	8.31	1.18	497.38	88.45	352	R	X
4	2003-274	2004-111	1798	2.11	0.33	24.03	55.92	123	X	R
7	2003-275	2004-113	5957	8.43	1.10	579.49	89.44	314	R	X
9	2003-275	2004-114	8073	13.71	1.73	332.71	87.99	317	R	X
Total			6787(mean)	11.21(mean)	1.36	329.04	81.83			
Deployment 2										
1	2004-103	2005-126	240	0.11	0.02	63.24	54.64	132	X	R
2	2004-103	2005-125	6162	4.23	0.64	225.00	80.41	319	X	X
3	2004-103	2005-125	13797	15.21	1.41	76.60	83.81	154	X	R
4	2004-103	2005-076	42	0.02	0.00	52.69	45.60	252	R	X
6	2004-102	2005-125	2422	1.49	0.24	36.61	58.14	331	R	X
8	2004-104	2005-127	12145	10.25	1.30	476.40	97.46	338	R	X
9*	2004-110	2005-070	3617	5.02	0.50	170.43	79.25	309	R	X
10	2004-101	2005-125	2743	1.33	0.28	30.27	58.96	323	R	X
11	2004-101	2005-127	13542	12.47	1.38	308.78	102.98	326	R	X
Total			6079(mean)	5.57(mean)	0.64	160.00	73.47			
Deployment 3										
4	2005-123	2006-115	6705	6.86	0.76	421.94	89.67	132	X	R
4-pre	2005-123	2006-022	6564	9.05	1.04	439.73	90.95	130	X	R
4-post	2006-023	2006-115	141	0.36	0.06	89.01	58.88	151	X	R
5*	2005-123	2006-115	11664	19.36	1.82	251.27	89.86	274	X	X
5-pre*	2005-123	2006-022	7030	17.56	1.67	266.71	90.96	275	X	X
5-post	2006-023	2006-115	4634	21.69	2.15	237.85	86.34	271	X	X
9	2005-121	2006-114	15359	25.35	1.68	842.75	104.90	300	R	X
9-pre	2005-121	2006-022	11977	27.05	1.88	896.79	106.02	301	R	X
9-post	2006-023	2006-114	3382	21.13	1.56	768.10	96.10	273	X	X
Total			11242(mean)	17.19(mean)	1.42	505.32	94.81			
Deployment 4										
1	2006-114	2007-014	3060	2.98	0.52	410.00	87.55	330	R	X
4	2006-114	2007-033	4323	6.01	0.55	309.28	85.32	176	X	X
7	2006-114	2007-032	12423	16.80	1.77	185.24	83.52	299	R	X
8	2006-114	2007-033	9557	11.31	1.36	134.83	78.44	317	X	X
10	2006-114	2007-032	14402	37.85	2.09	366.30	100.76	342	R	X
11	2006-114	2007-032	14482	21.82	2.09	364.61	89.68	355	R	X
12	2006-114	2007-033	4392	6.98	0.61	575.32	89.33	282	R	X
Total			8948(mean)	14.82(mean)	1.28	335.08	87.80			
All Deployments										
4	2003-274	2007-033	11605	15.00	0.40	201.98	69.13	139	X	R
9	2003-275	2006-114	27049	44.09	1.30	448.63	90.71	307	R	X
Composite	2003-274	2007-033	7713(mean)	10.90(mean)	1.08	289.45	82.06	319	X	X

* Did not record continuously

X= Temporally nonrandom occurrence (>99% significance)

R=Temporally random occurrence (>99% significance)

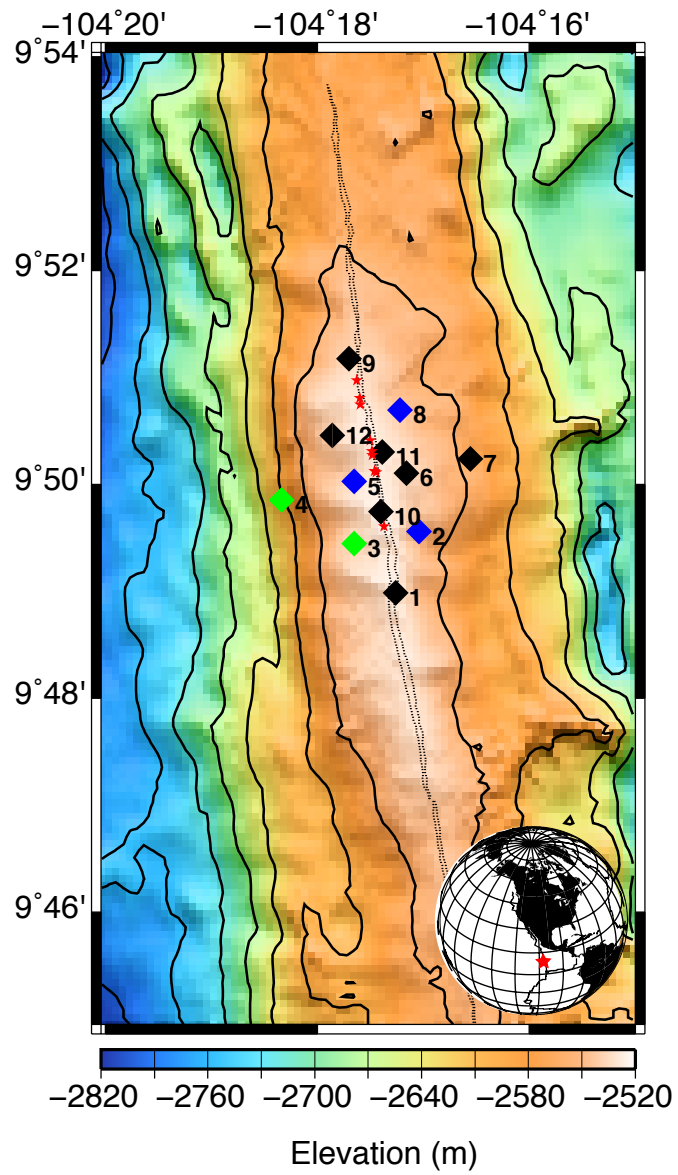


Figure 1. OBS Locations

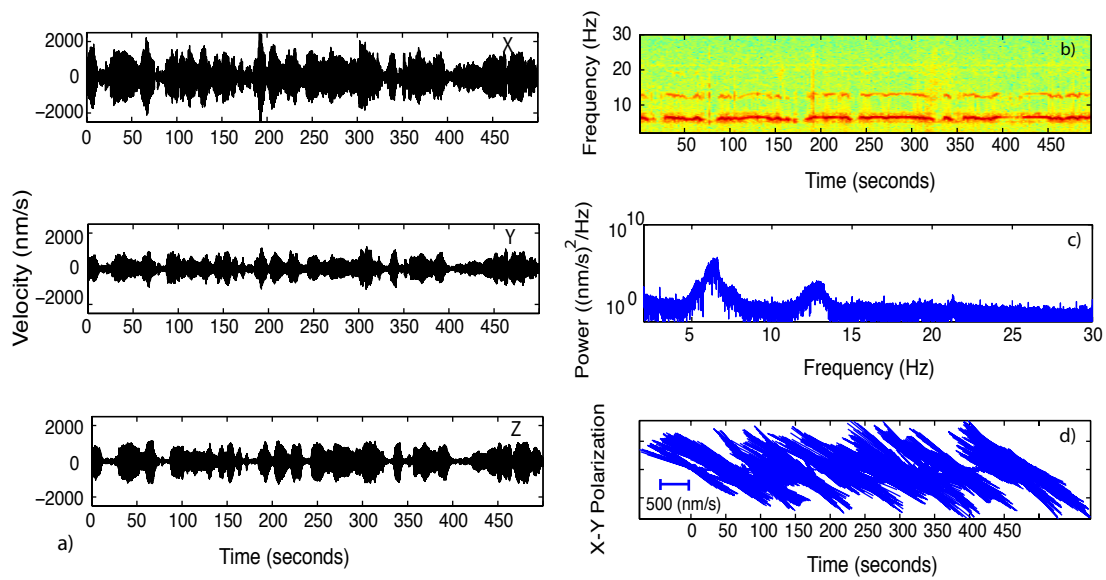


Figure 2. Spectral Signature

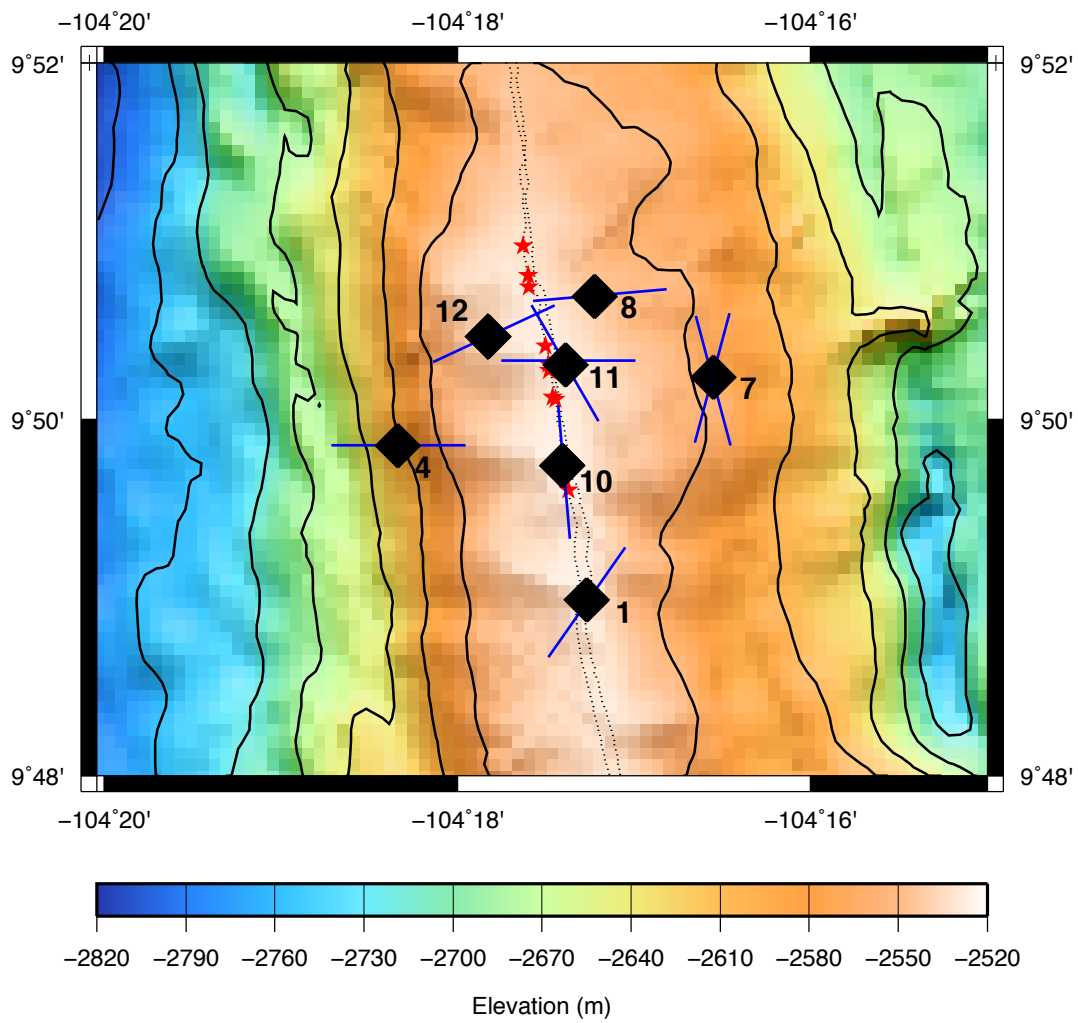


Figure 3. Tremor Polarization

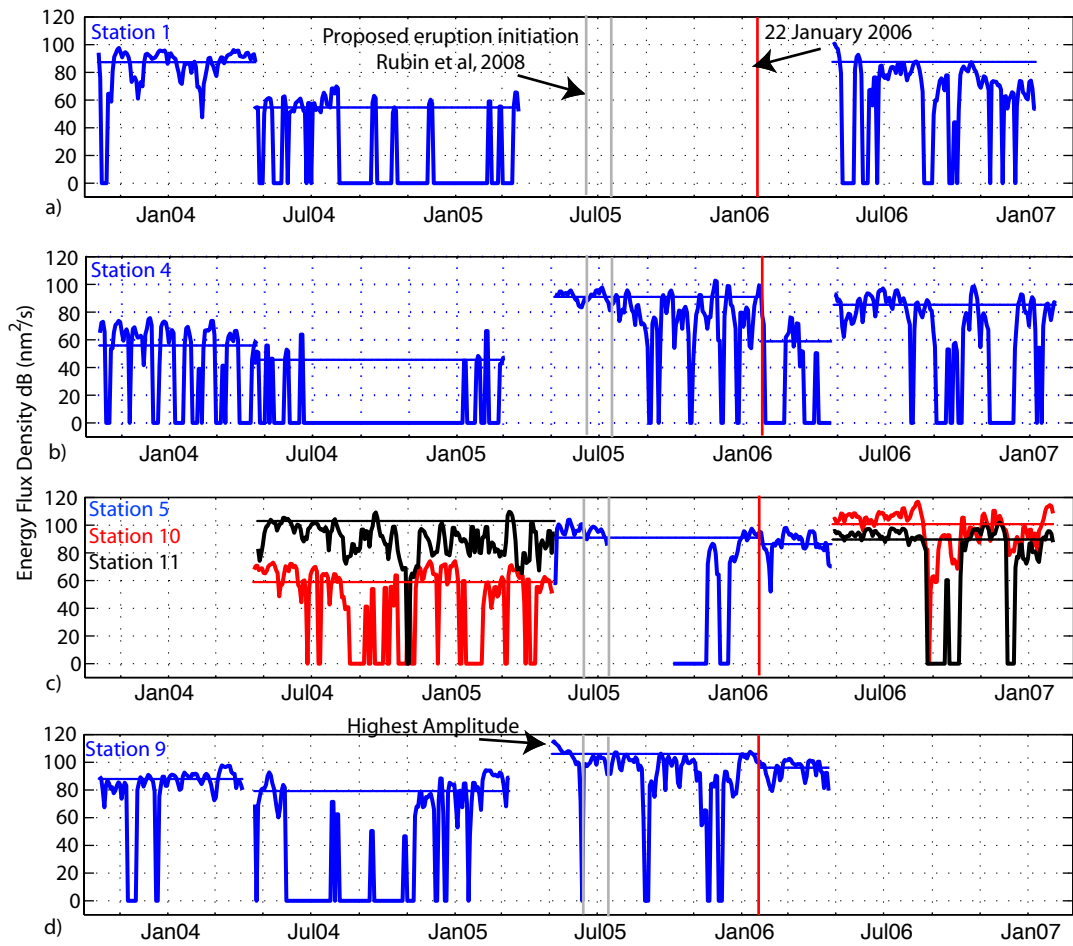


Figure 4. Energy Flux Density

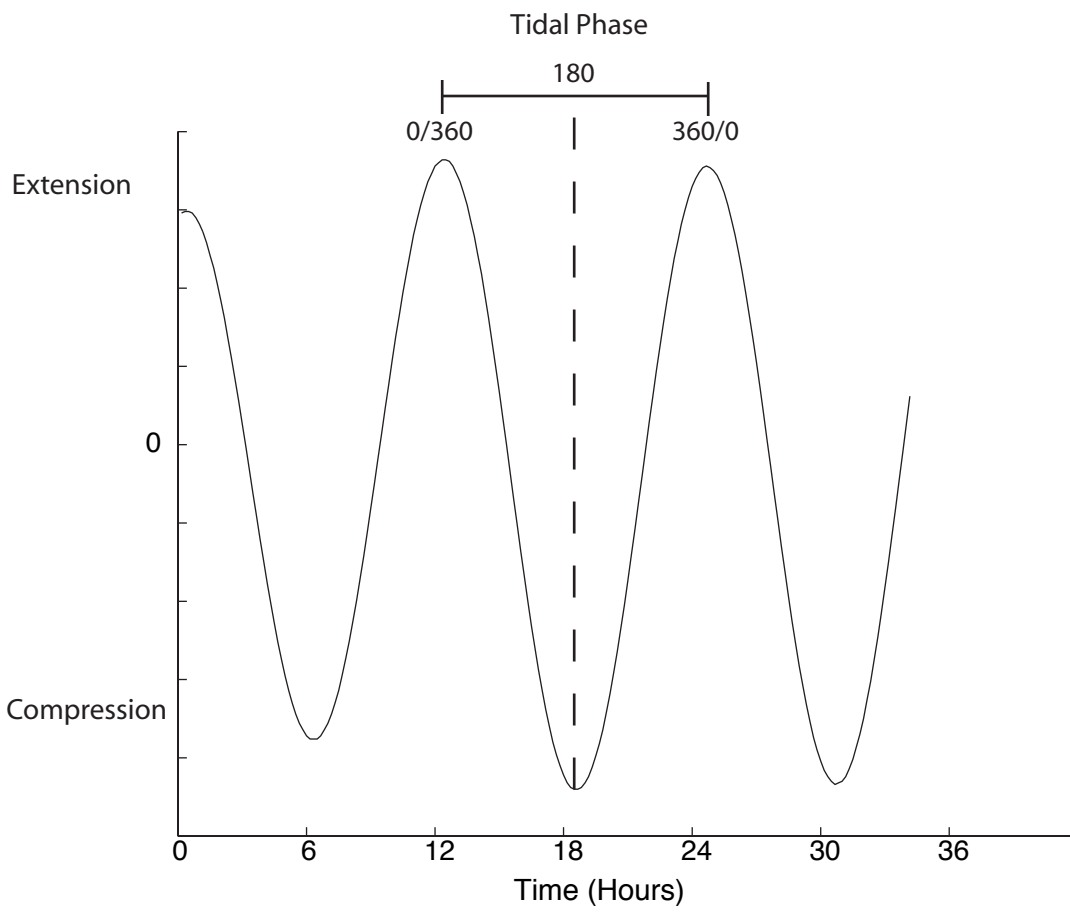


Figure 5. Tidal Phase

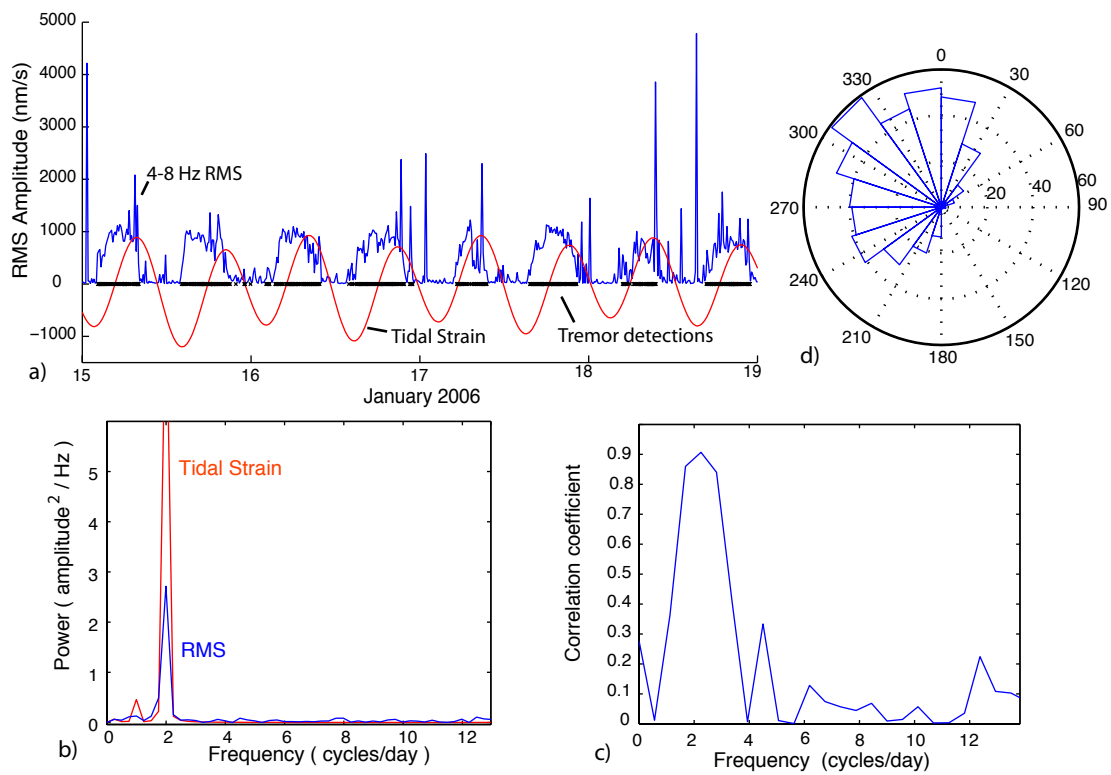


Figure 6. High Correlation Example

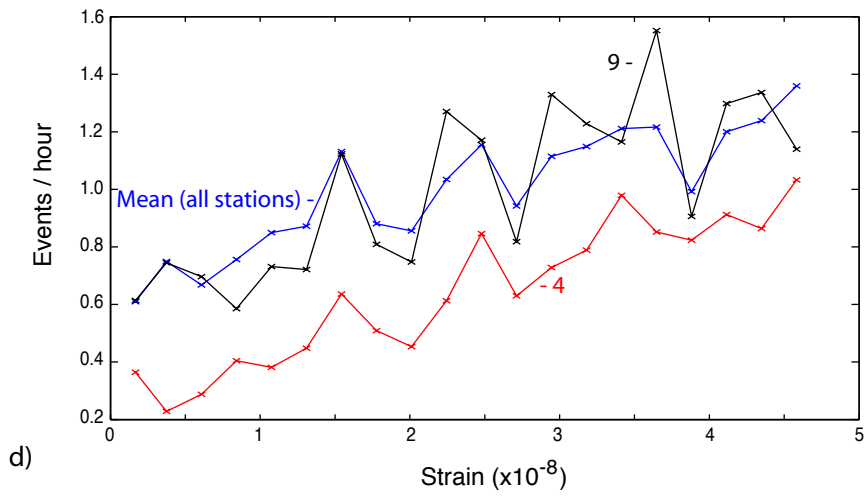
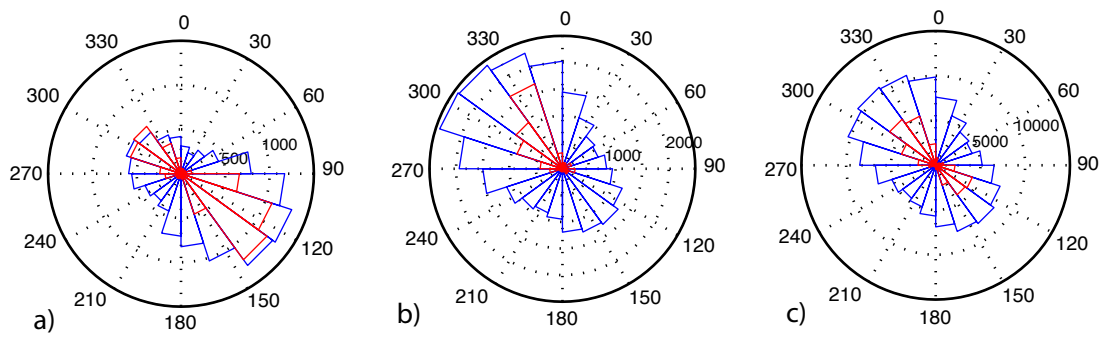
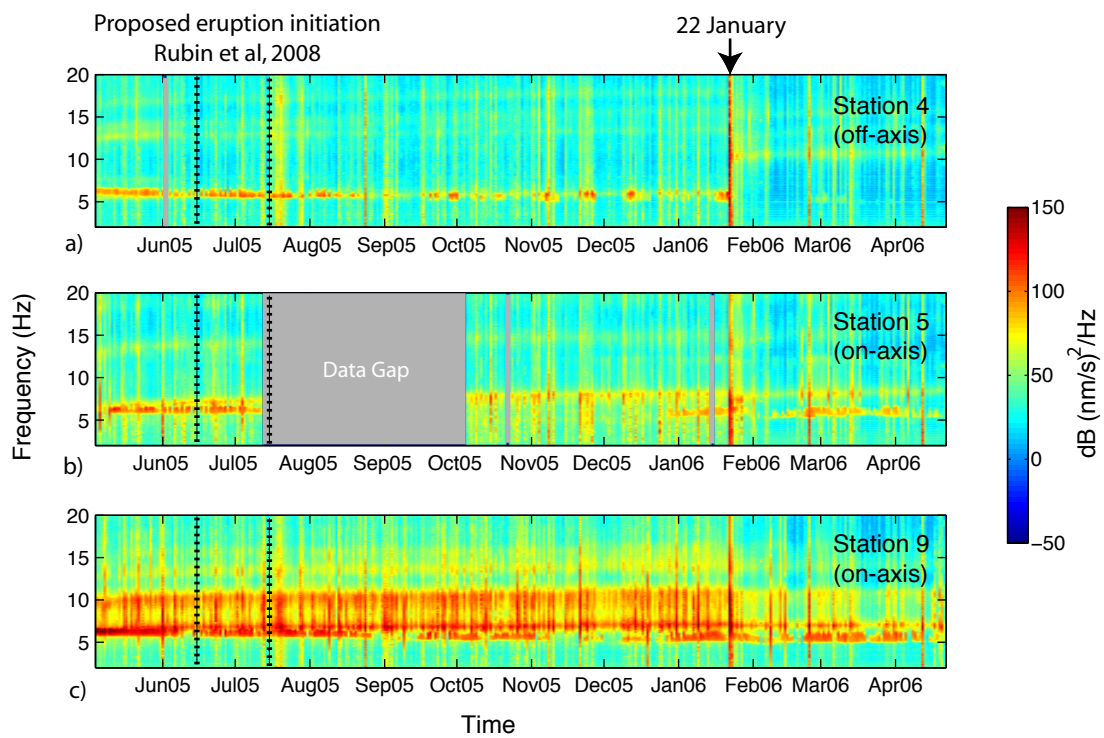


Figure 7. Tidal Influences



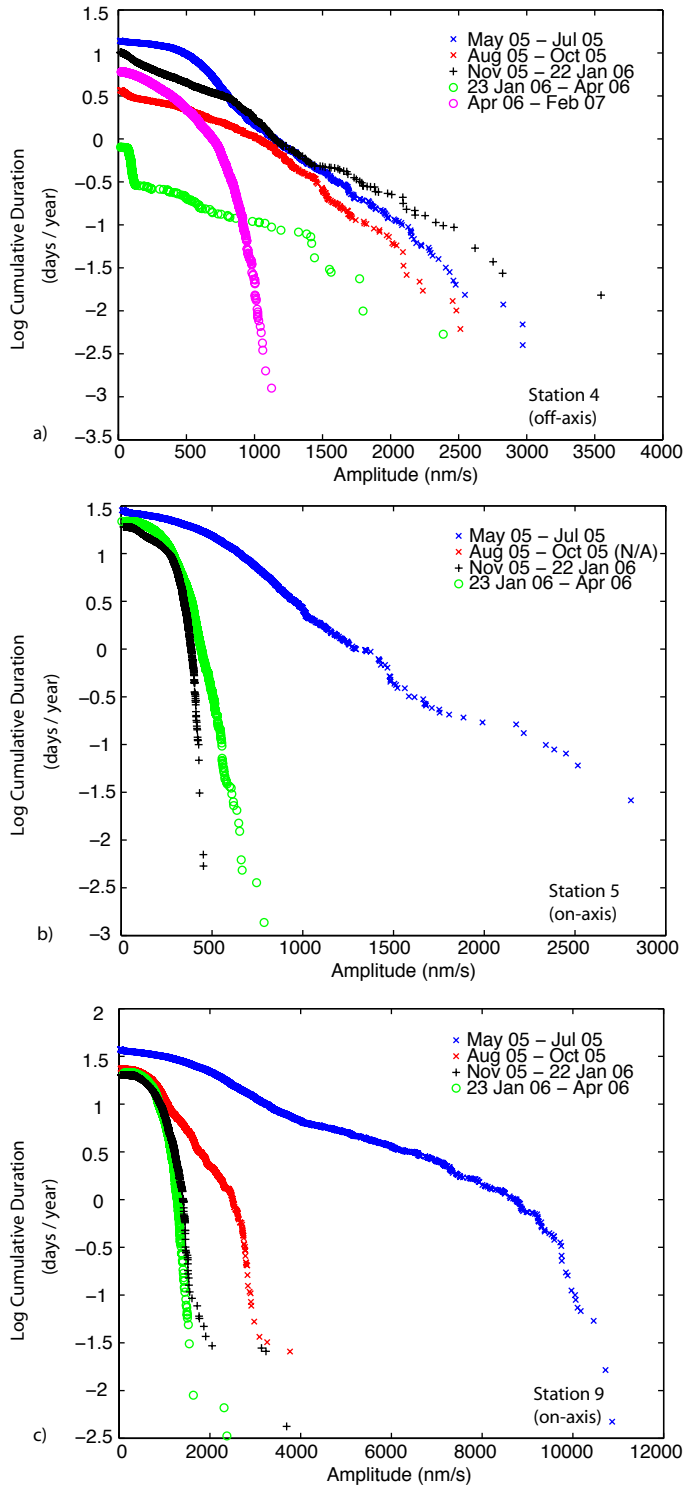


Figure 9. Duration-Amplitude Distributions

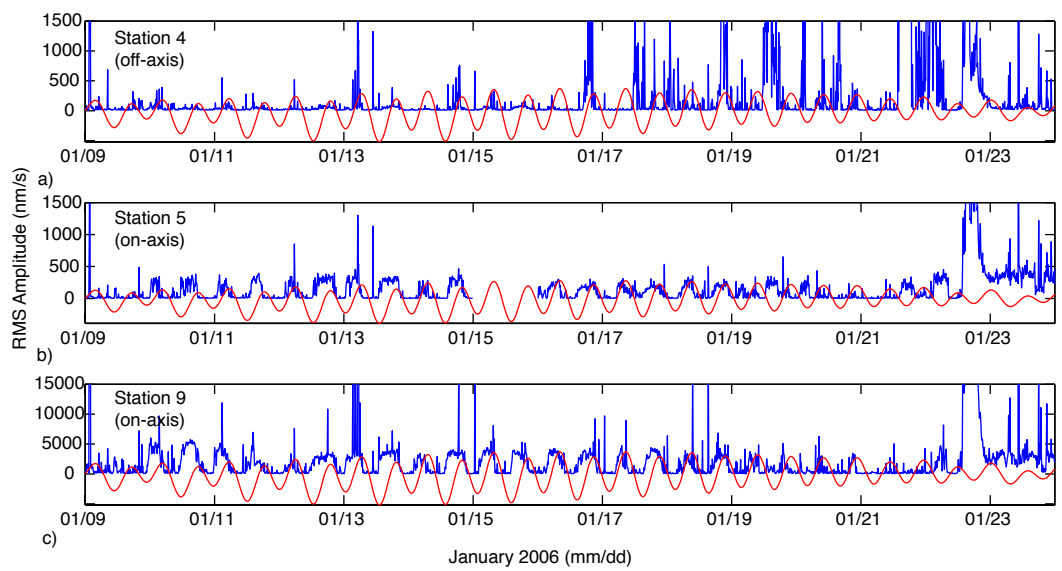


Figure 10. RMS Amplitudes Preceding Eruption

Appendices

Appendix 1: Supplemental Figures

Figure 1.

Kernel used for spectral correlation in *Ishmael* [Mellinger, 2002]. The kernel is 25 seconds in duration and approximates a hat function with equal regions of positive and negative to counteract background noise and broadband activity. The kernel is positive between 4-8 Hz, the bandwidth associated with tremor activity.

Figure 2.

Fast Fourier Transform (FFT) of ocean bottom current data [Adams et al., 2008] in blue, plotted with tidal strain, in red, and 4-8 Hz 10-minute RMS amplitudes in black. All FFT data are normalized by the standard deviation of the individual signals for plotting purposes. Ocean bottom currents exhibit a quarter diurnal periodicity, which is not evident in tremor activity, suggesting tremor is not a result of current driven noise or Karman vortex shredding [Duennebieer et al., 1981].

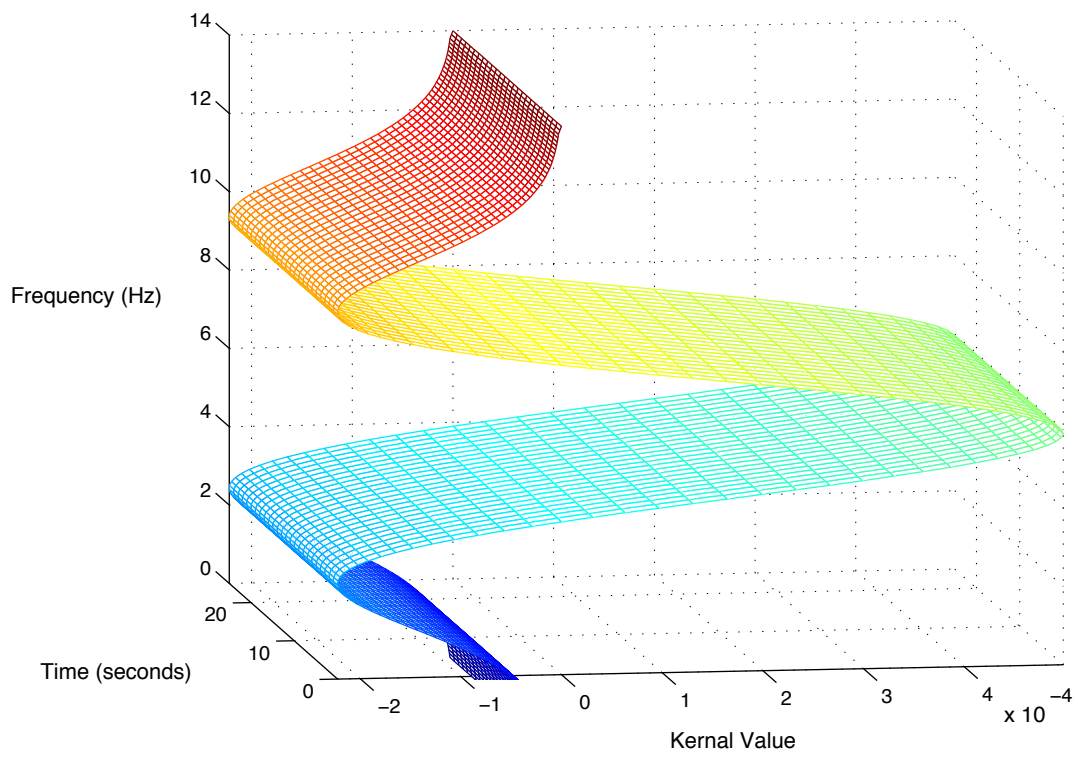


Figure 1

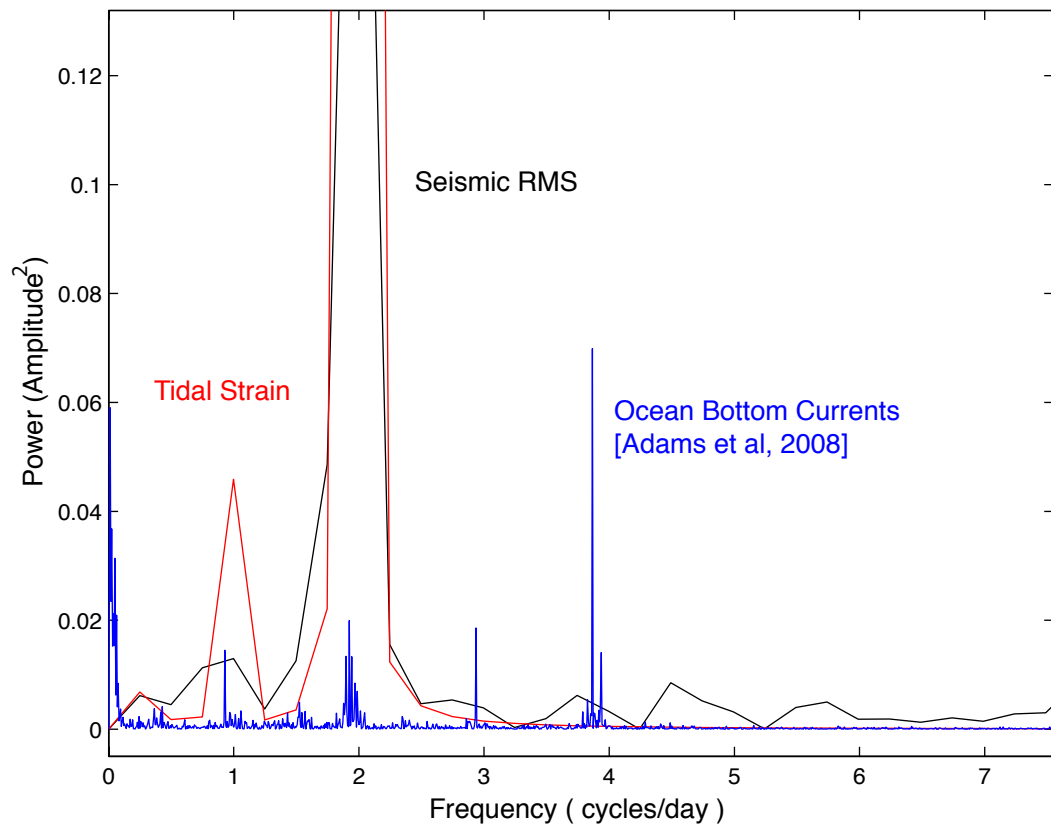


Figure 2

Appendix 2: Supplemental Table

Appendix 2. Ocean Bottom Seismometer Orientation Analysis

OBS	Latitude	Longitude	Orient-pred	Orient-calc	OBS-Correction
1	9.8166	-104.2849	28.53	352.76	35.77
4	9.8633	-104.3062	38.53	345.14	53.59
7	9.8363	-104.2754	35.45	2.20	33.25
8	9.8442	-104.2878	32.10	309.86	82.24
10	9.8281	-104.2879	30.30	12.71	17.59
11	9.8376	-104.2889	31.56	357.23	34.33
12	9.8411	-104.2971	33.65	353.29	40.36

EQ	MM/DD/YY	HHMMSS.SS	Lat	Long	Magnitude
1	7/30/06	234521.94	10.01	-104.22	5.4 (Mw)
2	8/21/06	184453.55	10.08	-104.07	4.4 (Mb)

* Earthquake information from USGS NEIC

* Orient-pred and Orient-calc are mean values for two listed earthquakes

* OBS-correction is degrees rotation clockwise

Appendix 3: Matlab Programs and Functions

```
% Creates daily average spectrogram for long-term analysis- example Figure
% 8

Pxx301=zeros(1025,1); %Creates empty matrix
[files]=textread('/R3/d_wav_obs/d_eprD4/site301_ch1.txt','%19c'); % Opens list of file names
for i=2:length(files)-1 % eliminates first and last file for noise purposes
    fname=files(i,1:19);
    [fid]=fopen(strcat('/R3/d_obs/d_eprD4/db/Site301/',fname), 'r','l');
    fseek(fid,0,-1);
    status=fseek(fid,240,'bof');
    y=fread(fid,'int');
    y=y*.257; % (nm/s)/count for deployments 3 & 4
    [Pxx,f]=pwelch(y,1440,0,[],125); % 1- hour windows, no overlap, default nfft
    Pxx301(:,i-1)=Pxx; % second file is first column
end

clear files
clear i
save avgfftD4.mat
```

```
% Used to evaluate temporal patterns and significance.
% Uses file with tremorphase picks to divide up by quadrant (x1=1:90;
% x2=91:180; x3=181:270; x4=271:360). Input column with degrees 0-360.

function [cdf]=binomialcheck(tremorphase)

a=find(tremorphase<=90);
b=find(tremorphase<=180 & tremorphase>=91);
c=find(tremorphase<=270 & tremorphase>=181);
d=find(tremorphase<=360 & tremorphase>=271);
e=length(tremorphase);

cdf(:,1)=1-binocdf(length(a),e,0.25);
cdf(:,2)=1-binocdf(length(b),e,0.25);
cdf(:,3)=1-binocdf(length(c),e,0.25);
cdf(:,4)=1-binocdf(length(d),e,0.25);
```

```

% Used to calculate RMS amplitude for each individual tremor event detected
% in Ishmael

% input time vector [yr,mon,dt,stsc,etsc,datenum], td is file with start times for each data file (yr,mon,κ
day,datenum)
% output is [std(x),std(y),std(z),datenum]
% Must make sure files and td start on same DAY! & D4 is Little Endian not
% Big Endian

function [xyz_time]=xyztrem(time,td)
[ydw,t,samprate]=return_yt_seguint32('/R3/d_obs/d_eprD3/db/Site209-Longview/2006-01-01_S209-Longview_ch1',κ
2006,001,01,52,35,125*30);
w=1:720000:10800000; % Divides file into largest possible data segments to be xcorr with datawrite
w(16)=10799750; % Drops last 2 seconds to ensure no error if file is not full length
f=1;
[files_z]=textread('/R3/d_wav_obs/d_eprD4/site310_ch1.txt','%19c');
[files_x]=textread('/R3/d_wav_obs/d_eprD4/site310_ch2.txt','%19c');
[files_y]=textread('/R3/d_wav_obs/d_eprD4/site310_ch3.txt','%19c');
for k=1:length(td(:,1))
q=find(time(:,6)==td(k,4)); % find if file has tremor detection and how many- used later in script
if isempty(q)==0 % If there is a tremor detection, open and read files for x,y,z
    fname=files_z(k,1:19);
    [fid]=fopen(strcat('/R3/d_obs/d_eprD4/db/Site310/',fname), 'r','l');
    fseek(fid,0,-1);
    status=fseek(fid,240,'bof');
    z=fread(fid,'int');
    z=z-mean(z); % Ensure that mean is 0
    dz=bandpass(z,4,8,length(z),1/125); % bandpass between 4 and 8 Hz

    fname=files_x(k,1:19);
    [fid]=fopen(strcat('/R3/d_obs/d_eprD4/db/Site310/',fname), 'r','l');
    fseek(fid,0,-1);
    status=fseek(fid,240,'bof');
    x=fread(fid,'int');
    x=x-mean(x);
    dx=bandpass(x,4,8,length(x),1/125);

    fname=files_y(k,1:19);
    [fid]=fopen(strcat('/R3/d_obs/d_eprD4/db/Site310/',fname), 'r','l');
    fseek(fid,0,-1);
    status=fseek(fid,240,'bof');
    y=fread(fid,'int');
    y=y-mean(y);
    dy=bandpass(y,4,8,length(y),1/125);

    for j=1:15
        u=z(w(j):w(j+1));
        [c,lags]=xcorr(ydw,u,'none'); %cross correlates to check for datawrites
        a=find(c>=1.5e10); % If correlation is greater than this value- datawrite present
        if a>0 % If datawrite exists...
            b=max(c);
            c=find(c==b);
            q=abs(lags(c));
            dz(w(j)+g:w(j)+g+7500)=NaN; % Removes 60 seconds of data beginning at datawrite
            dx(w(j)+g:w(j)+g+7500)=NaN;
            dy(w(j)+g:w(j)+g+7500)=NaN;
        end
    end

    for v=1:length(q) % number of tremor events within file
        xyz_time(f,1)=nanstd(dx(floor(time(q(v),4)*125):floor(time(q(v),5)*125))*0.257);
        xyz_time(f,2)=nanstd(dy(floor(time(q(v),4)*125):floor(time(q(v),5)*125))*0.257);
        xyz_time(f,3)=nanstd(dz(floor(time(q(v),4)*125):floor(time(q(v),5)*125))*0.257);
        xyz_time(f,4)=datenum(time(f,1),time(f,2),time(f,3),0,0,time(f,4)); % Time stamp of κ
event
        f=f+1;
    end

    clear q;
end
if k==100
    save xyztrem310.mat
elseif k==200
    save xyztrem310.mat
end
k=k+1; % Next file
end

```

```

% Calculates 10-minute RMS amplitudes in 4-8 Hz bandwidth- Example Figure
% 10

q=1:75000:10800000; % Divides file into 10-minute segments
q(145)=10799750; % Accounts for inconsistencies in lengths of files
w=1:720000:10800000; % Longest possible divisions for datawrite xcorr
w(16)=10799750;
f=1; % Start at datapoint 1

[ydw,t,samprate]=return_yt_segint32('/R3/d_obs/d_eprD3/db/Site209-Longview/2006-01-01_S209-Longview_ch1',
2006,001,01,52,35,125*30); % Sample datawrite

[files]=textread('/R3/d_wav_obs/d_eprD4/site312_ch1.txt','%19c');
for i=2:length(files)-1 % Skips first and last file for noise reasons
    fname=files(i,1:19);
    [fid]=fopen(strcat('/R3/d_obs/d_eprD4/db/Site312/',fname), 'r','l');
    fseek(fid,0,-1);
    status=fseek(fid,240,'bof');
    y=fread(fid,'int');
    y=y-mean(y); % Makes mean 0
    d=bandpass(y,4,8,length(y),1/125);

    for j=1:15 %Checks each segment for datawrite
        x=y(w(j):w(j+1));

        [c,lags]=xcorr(ydw,x,'none');
        a=find(c>=1.5e10); % if xcorr correlation is higher than this value- datawrite present
        if a>0
            b=max(c);
            c=find(c==b);
            g=abs(lags(c)); % Locates beginning of datawrite
            d(w(j)+g:w(j)+g+7500)=NaN; % Replaces with NaN
        end
    end

for k=1:144 % Calculates 10 minute RMS average of file with datawrites removed
    if k==1
        rmsVel(f,2)=return_datenum_segint32(strcat('/R3/d_obs/d_eprD4/db/Site312/',fname)); %Datenum from file
    header
    end

    z=d(q(k):q(k+1));
    v=y(q(k):q(k+1));

    [c,lags]=xcorr(ydw,v,'none'); % Double check for datawrite in 10 min clip
    a=find(c>=1.5e10);
    if a>0
        b=max(c);
        c=find(c==b);
        g=abs(lags(c));
        z(g:g+7500)=NaN;
        if length(z)>=75010
            p=length(z)-75001;
        end
    end

    rmsVel(f,1)=nanstd(z)*.257;

f=f+1; % Next 10 min clip within file

end
end

disp('end 312')
save rmsVel312.mat

```

```
% Calculates duration-amplitude distribution normalized by deployment
% length- Example Figure 9

% Input x=[duration,amplitude,floor(datenum)]- output is [amplitude,cumulative
% duration]; Cumulative duration is in days/year monitoring

function y=duramp_dist(x)
[y,i]=sort(x(:,2)); % Sorts data in ascending order
y(:,2)=x(i,1); % Writes durations in order of ascending RMS
c=cumsum(flipud(y(:,2))); % Cumulative sum of flipped durations to get duration above each amplitude
d=x(length(x(:,1)),3)-x(1,3); % Finds time in days from beginning of trem detections to end of trem
detections
c=(c/86400)/(d/365); % Converts duration (seconds) to days and normalizes based on monitoring
duration/year
y(:,2)=flipud(c); % Re-orders in association with each trem event

% figure;plot(y(:,1),log10(y(:,2)),'x');xlabel('Amplitude (nm/s)');ylabel('Log cumulative duration
(days/year monitoring)')
```

```

% Calculates tidal correlation in 10-minute RMS averages and temporal lag
% behind peak tidal strains- in degrees. Example Figure 7a,b,b- red values

% Input tidalvs= [time,strain], rms=[RMS amplitude,time]

function [avgrad]=lagcheck(tidalvs,rms)

avgrad(1,1:5)=NaN;

p=1;
t=0:144:56488; % Creates vector counting by 144 starting at 1- end number is higher than longest file
t(1)=1;
a=length(rms(:,1));
b=find(t==a); % Uses this to cut t to size vector needed for analysis
c=find(tidalvs(:,1)==round(rms(1,2))); % Finds tidal start time associated with 10-min average start time
d=find(tidalvs(:,1)==round(max(rms(:,2)))); % Finds tidal end time associated with 10-min average end time
tidalvs1(:,1)=tidalvs(c:d,1); %Writes new tidal strain file that matches timing of RMS file
tidalvs1(:,2)=tidalvs(c:d,2);

for k=1:2:b-5 % Counts by 144 (one day of RMS averages) to 5 from the last day- to account for 4-day
window
[Cxy,f]=mscohere(tidalvs1(t(k):t(k+4),2),rms(t(k):t(k+4),1),144,77,512,1/600); % Correlation
coefficient
a=find(Cxy(8:9)>=0.5); % If greater than 50% correlation, find phase angle below
if a>0
[Pxy,F]=cpsd(tidalvs1(t(k):t(k+4),2),rms(t(k):t(k+4),1),144,77,512,1/600);
phase=angle(Pxy);
prad=interp1(F,phase,1/43200); % interpolates phase lag associated with 2 cycles/day frequency
avgrad(p,1)=prad; % Records phase lag from above
avgrad(p,2)=t(k); % Records data point start number
avgrad(p,3)=prad*(360/(2*pi)); % Records degrees lag
avgrad(p,4)=max(Cxy); % Records correlation coefficient
avgrad(p,5)=prad; % converts lag to 0-360 degrees from -180 to 180
if prad<=0
avgrad(p,5)=prad+2*pi;
end
avgrad(p,6)=tidalvs1(t(k),1); % Datenum associated with start time
p=p+1;
end
end

if avgrad(1,2)>0 % IF tidal correlations exist in RMS Data...
[T,R]=rose(avgrad(:,5));figure;polar(T,R);view(90,-90); % Create rose diagram
end

```

```
% orientation_pred- uses OBS location with USGS EQ to
% predict the azimuth to the EQ location; orient_calc uses p-wave
% polarizations to calculate arrival azimuth before obs calibration;
% orient_adj is adjusting the orient_calc so that 360 degrees is actually
% 90, so that orientation_pred and orient_calc are on the same axis; orient
% fix is orient_adj-orient_pred, to get average azimuth adjustment
% necessary to line up OBS p-wave arrival with actual orientation of EQ!
% Orient_fix (:,4) are mean adjustments required to orient obs
% instrumentation in degrees clockwise adjustment - Used for Figure 3 and
% supplemental table in appendix 2

% Degrees clockwise from North
for i=1:7
for j=1:3
orient_pred(i,j)=azimuth(obsloc(i,2),obsloc(i,3),gseq(j,2),gseq(j,3),'degrees');
end
end

% In order for angles approaching 360 to be seen as negative to zero
for i=1:7
for j=1:3
orient_adj(i,j)=orient_calc(i,j);
if orient_calc(i,j)>=270
orient_adj(i,j)=(orient_adj(i,j)-360);
end
end
end

% positive fix is adding degrees from north to east (more positive azimuth)
for i=1:7
for j=1:3
orient_fix(i,j)=orient_pred(i,j)-orient_adj(i,j);
end
end

orient_fix(1,4)=mean(orient_fix(1,1:3));
orient_fix(2,4)=mean(orient_fix(2,1:3));
orient_fix(4,4)=mean(orient_fix(4,1:3));
orient_fix(3,4)=mean(orient_fix(3,2:3));
orient_fix(5,4)=mean(orient_fix(5,1:3));
orient_fix(6,4)=mean(orient_fix(6,1:3));
orient_fix(7,4)=mean(orient_fix(7,1:3));
```

```

% Used to calculate tremor azimuth- Figure 3. Used in conjunction with
% corrections in Appendix 3.

% input time vector [yr,mon,dt,stsc,etsc,datenum], output is
% [datenum,p-value,mean theta radians, mean theta degrees, r vector]
% Must make sure files and td start on same DAY!- shoo from
% $/tidaltremor/d_tremorstats

function [xy_data]=xy_angle(time,td)
[ydw,t,samprate]=return_yt_seguint32('/R3/d_obs/d_eprD3/db/Site209-Longview/2006-01-01_S209-Longview_ch1',k,
2006,001,01,52,35,125*30);
w=1:720000:10800000; % For use with identifying datawrites
w(16)=10799750;
f=1;
[files_x]=textread('/R3/d_wav_obs/d_eprD4/site312_ch2.txt','%19c');
[files_y]=textread('/R3/d_wav_obs/d_eprD4/site312_ch3.txt','%19c');
[files_z]=textread('/R3/d_wav_obs/d_eprD4/site312_ch1.txt','%19c');
for k=1:length(td(:,1))
q=find(time(:,6)==td(k,4)); % If data file has tremor detections- open files
if isempty(q)==0
    fname=files_z(k,1:19);
    [fid]=fopen(strcat('/R3/d_obs/d_eprD4/db/Site312/',fname), 'r','l');
    fseek(fid,0,-1);
    status=fseek(fid,240,'bof');
    z=fread(fid,'int');
    z=z-mean(z);
    dz=bandpass(z,4,8,length(z),1/125);

    fname=files_x(k,1:19);
    [fid]=fopen(strcat('/R3/d_obs/d_eprD4/db/Site312/',fname), 'r','l');
    fseek(fid,0,-1);
    status=fseek(fid,240,'bof');
    x=fread(fid,'int');
    x=x-mean(x);
    dx=bandpass(x,4,8,length(x),1/125);

    fname=files_y(k,1:19);
    [fid]=fopen(strcat('/R3/d_obs/d_eprD4/db/Site312/',fname), 'r','l');
    fseek(fid,0,-1);
    status=fseek(fid,240,'bof');
    y=fread(fid,'int');
    y=y-mean(y);
    dy=bandpass(y,4,8,length(y),1/125);

    for j=1:15 % Find data writes
        u=z(w(j):w(j+1));
        [c,lags]=xcorr(ydw,u,'none');
        a=find(c>=1.5e10);
        if a>0 % If datawrite detected with cross correlation
            b=max(c);
            c=find(c==b);
            g=abs(lags(c));
            dz(w(j)+g:w(j)+g+7500)=NaN; % Replace datawrite with NaN
            dx(w(j)+g:w(j)+g+7500)=NaN;
            dy(w(j)+g:w(j)+g+7500)=NaN;
        end
    end

    for v=1:length(q)
        dxx=dx(floor(time(q(v),4)*125):floor(time(q(v),5)*125)).*257; % Dxx is bandpassed
        signal converted to
        nm/s of tremor detection
        dyy=dy(floor(time(q(v),4)*125):floor(time(q(v),5)*125)).*257;
        theta=atan(dxx./dyy); % Calculates theta value for length of tremor detection between
        -90 to 90 -not 0-360
        [p,mntheta,r]=shoo(theta); % Calculates Schuster p-value, mean theta, and r (length
        vector associated with Schuster P-value)
        xy_data(f,1)=datenum(time(f,1),time(f,2),time(f,3),0,0,time(f,4)); % Time stamp
        xy_data(f,2)=p; % Records p-value (significance level)
        xy_data(f,3)=mntheta(:,1); % Records theta degrees
        xy_data(f,4)=mntheta(:,2); % Records theta radians
        xy_data(f,5)=r;
        clear dxx
        clear dyy
        clear theta
        f=f+1;
    end

    clear q;
end
k=k+1;
end

```